

2/2020

Berlin



Deutscher Wissenschaftsherold



German Science Herald

Inter
GING

Bibliografische Information der Deutschen Nationalbibliothek

Die Deutsche Nationalbibliothek verzeichnet diese Publikation in der Deutschen Nationalbibliografie; detaillierte bibliografische Daten sind im Internet über <http://dnb.dnb.de> abrufbar.

Bibliographic information published by the Deutsche Nationalbibliothek

The Deutsche Nationalbibliothek lists this publication in the Deutsche Nationalbibliografie; detailed bibliographic data are available on the Internet at <http://dnb.dnb.de> .

Information bibliographique de la Deutsche Nationalbibliothek

La Deutsche Nationalbibliothek a répertorié cette publication dans la Deutsche Nationalbibliografie; les données bibliographiques détaillées peuvent être consultées sur Internet à l'adresse <http://dnb.dnb.de> .

Informazione bibliografica della Deutsche Nationalbibliothek

La Deutsche Nationalbibliothek registra questa pubblicazione nella Deutsche Nationalbibliografie; dettagliati dati bibliografici sono disponibili in internet in <http://dnb.dnb.de> .

Библиографическая информация Немецкой Национальной Библиотеки

Немецкая Национальная Библиотека вносит эту публикацию в Немецкую национальную библиографию; подробные библиографические данные можно найти в интернете на странице: <http://dnb.dnb.de> .

Información bibliográfica de la Deutsche Nationalbibliothek

La Deutsche Nationalbibliothek recoge esta publicación en la Deutsche Nationalbibliografie. Los datos bibliográficos están disponibles en la dirección de Internet <http://dnb.dnb.de> .

ISSN 2509-4327 (print)
ISSN 2510-4780 (online)



Deutscher Wissenschaftsherold German Science Herald

№ 2/2020

Die Zeitschrift „Deutscher Wissenschaftsherold“ ist eine Veröffentlichung mit dem Ziel ein breites Spektrum der Wissenschaft allgemeinverständlich darzustellen. Die Redaktionsleitung versteht sich als Vermittler zwischen Wissenschaftlern und Lesern. Durch die populärwissenschaftliche Bearbeitung wird es möglich unseren Lesern neue wissenschaftliche Leistungen am besten und vollständigsten zu vermitteln. Es werden Untersuchungen, Analysen, Vorlesungen, kurze Berichte und aktuelle Fragen der modernen Wissenschaft veröffentlicht.

Impressum

Deutscher Wissenschaftsherold – German Science Herald

Wissenschaftliche Zeitschrift

Herausgeber:

InterGING

Wiesenwinkel 2,
31785 Aerzen

Inhaber: Marina Kisiliuk

Tel.: + 49 5154 567 2017

Fax.: +49 5154 567 2018

Email: info@dwherold.de

Internet: www.dwherold.de

Chefredakteur:

Prof. Zamiatin P.M.

Korrektur:

O. Champela

Gestaltung:

N. Gavrilets

Auflage: № 2/2020 (September) – 20

Redaktionsschluss September, 2020

Erscheint vierteljährlich

Editorial office: InterGING

Wiesenwinkel 2,

31785 Aerzen

Tel.: + 49 5154 567 2017

Fax.: +49 5154 567 2018

Email: info@dwherold.de

Deutscher Wissenschaftsherold – German Science Herald is an international, German/English language, peer-reviewed journal and is published quarterly.

№ 2/2020

Passed in press in September, 2020

Druck: WIRMachenDRUCK GmbH

Mühlbachstr. 7

71522 Backnang

Deutschland

Der Abdruck, auch auszugsweise, ist nur mit ausdrücklicher Genehmigung der InterGING gestattet. Die Meinung der Redaktion oder des Herausgebers kann mit der Meinung der Autoren nicht übereinstimmen. Verantwortung für die Inhalte übernehmen die Autoren des jeweiligen Artikels.

INDEXING: Index Copernicus, Google Scholar, Ulrich's Periodicals Directory, Fachzeitschriften, MIAR.



© InterGING

© Deutscher Wissenschaftsherold – German Science Herald

REDAKTIONSKOLLEGIUM / INTERNATIONAL EDITORIAL BOARD:

Jurga Bernatoniene, Dr., Prof.
Physics, Lithuania,
jurgabernatoniene@yahoo.com

Arvidas Galdikas, Dr. habil., Prof.
Physics, Lithuania,
arvidas.galdikas@ktu.lt

Kristina Ramanauskienė, Ph.dr., Prof.
Pharmacy, Lithuania,
kristinaraman@gmail.com

Khпалиuk Alexander, Dr. med. habil., Prof.
Pharmakologie, Belarus,
clinicfarm@bsmu.by

Arnold M. Gegechkori, Dr., full Prof.
Biology, Georgia,
arngegechkori@yahoo.com

Omari Mukbaniani, Prof., DSc.
Chemistry, Georgia,
omar.mukbaniani@tsu.ge

Teimuraz Lezhava, Prof.
Genetics, Georgia,
teimuraz.lezhava@tsu.ge

Shota A. Samsoniya, Prof.
Chemistry, Georgia,
shota.samsonia@tsu.ge

Mdzinarashvili Tamaz, DSc., Prof.
Biophysics, Georgia,
tamaz.mdzinarashvili@tsu.ge

Aliaksandr V.Prokharau, MD, PhD, MSc., Prof.
Oncology, Belarus,
aprokharau@gmail.com

Pyrochkin V., MD, PhD, MSc., Prof.
Theraphy, Belarus,
wlad_cor@mail.ru

Golubev A.P., BD, Prof.
Ecology, Belarus,
algiv@rambler.ru

Makarevich A., MD, PhD, Prof.
Theraphy, Belarus,
makae@bsmu.by

Kanunnincova N., BD, Prof.
Physiology, Belarus,
n.kanunnikova@grsu.by

Giedrius Vanagas, Prof.
Internal Medicine, Lithuania,
Giedrius.Vanagas@ismuni.lt

Armuntas Baginskas, Prof.
Neurofiziologija, Lithuania,
Armuntas.Baginskas@ismuni.lt

Ricardas Radisauskas, MD., Ph.D., Prof.
Cardiology, Lithuania,
Ricardas.Radisauskas@ismuni.lt

Meyramov Gabit, Prof.
Cytology and Histology, Kazakhstan,
meyramow@mail.ru

Aisha Mohammed Abd al-salam Shahlol,
Ph.D. in Medical Bacteriology, Libya,
Ais.shahlol@sebhau.edu.ly

Edmundas Kadusevicius, MD, PharmD, PhD, Prof.
Pharmacology, Lithuania,
Edmundas.Kadusevicius@ismuni.lt

Ivo Grabchev, Prof., PhD.
Chemistry, Bulgaria,
i.grabchev@chem.uni-sofia.bg
grabchev@mail.bg

Mariyana Ivanova Lyubenova, Prof., PhD.
Ecology, Bulgaria,
ryann@abv.bg
ryana_1@yahoo.com

Tsvetanka Tsankova Marinova, MD, PhD, DMedSci.
Biology, Bulgaria,
tmarinova@yahoo.com

Evgueni D. Ananiev, Prof., PhD.
Biology, Bulgaria,
evgueni_ananiev@yahoo.com

Plamen G. Mitov, Prof., PhD.
Biology, Bulgaria,
mitovplamen@gmail.com

Atanas Dimov Arnaudov, PhD.
Physiology, Bulgaria,
arny87@yahoo.co.uk

Iliana Georgieva Velcheva, PhD.
Ecology, Bulgaria,
anivel@abv.bg

Osman Demirhan, Prof.
Biology, Turkey,
osdemir@cu.edu.tr

Jharna Ray, M. Sc., PhD, Prof.
Neurogenetics, India,
Indiaharnaray@gmail.com

Marián Halás doc. RNDr, PhD.
Human geography, Czech,
marian.halas@upol.cz

Ayfer Pazarbasi Prof. Dr.
Biology, Turkey,
payfer@cu.edu.tr

Tusharkanti Ghosh Prof.
Physiology, India,
tusharkantighosh53@yahoo.in

Khudaverdi Ganbarov, Prof.
Microbiology, Azerbaijan,
khuda1949@mail.ru

Rovshan Ibrahimkhalil Khalilov, Prof.
Biophysics, Azerbaijan,
hrovshan@hotmail.com

Meyramov G.G., Prof.
Diabetology, Kazakhstan,
meyramow@mail.ru

Svitlana Antonyuk, Dr.phil.
Stony Brook University, USA
Linguistics

Samuel M.Johnson, Prof. Dr. phil.
Theology, Wells, Maine, USA,
djtjohnson@earthlink.net

Satanovsky Leon, MD, PhD.
Perio-odontologie, Israel,
satleonid@gmail.com

Pohorielova O.O.

PhD student of the Department of Phthysiology and Pulmonology of Kharkiv National Medical University, Kharkiv, Ukraine,
61062, Department of Phthysiology and Pulmonology of Kharkiv National Medical University, Nauky prosp. 4, Kharkiv,
Ukraine, evildevilolga@gmail.com

Shevchenko O.S.

MD, Professor, Head of the Department of Phthysiology and Pulmonology of Kharkiv National Medical University, Kharkiv,
Ukraine 61062, Department of Phthysiology and Pulmonology of Kharkiv National Medical University, Nauky prosp. 4,
Kharkiv, Ukraine, diva5002007@yahoo.com

DEPENDENCE OF HUMAN-BETA-DEFENSIN-1 LEVEL ON DRUG-RESISTANCE SPECTRUM AND TREATMENT REGIMENS IN PATIENTS WITH PULMONARY TUBERCULOSIS

Abstract. Taking into account the constant expansion of *M. tuberculosis* drug resistance, the study of the host immune response components, which can be used in diagnosis, prediction of tuberculosis course and pathogenetic treatment, is becoming an increasingly urgent issue. The purpose of the study was to compare Human-beta-defensin-1 level in different types of drug-resistance in patients with pulmonary tuberculosis and its dynamics during use of standard and individualized regimens of anti-tuberculosis treatment. **Materials and methods.** 100 patients with tuberculosis were included in the study. Human-beta-defensin-1 (HBD-1) level was measured in all the patients at the treatment onset and 2 months later. The patients also underwent chest X-ray, sputum smear microscopy, sputum molecular-genetic study, sputum culture on liquid and solid media, blood count, blood biochemistry. Patients were treated with standard and individualized anti-tuberculosis treatment regimens. Statistical data processing was carried out using Statistica 8.0. **Results:** After 2 months of anti-tuberculosis treatment HBD-1 level was significantly higher in patients with drug-resistance ($42.1 \pm 8.2 \mu\text{mol/L}$, median – $16.8 \mu\text{mol/L}$) than in patients with drug-susceptible tuberculosis ($15.9 \pm 5.3 \mu\text{mol/L}$, median – $38.4 \mu\text{mol/L}$), and there was a significant ($p < 0.05$) difference between HBD-1 levels in patients with different types of drug-resistance with its increase in wider resistance spectrum: in mono-resistant TB – $12.6 \pm 5.8 \mu\text{mol/L}$ (median – $12.0 \mu\text{mol/L}$), in MDR-TB – $38.1 \pm 6.9 \mu\text{mol/L}$ (median – $56.2 \mu\text{mol/L}$), in XDR-TB – $71.8 \pm 28.5 \mu\text{mol/L}$ (median – $104.8 \mu\text{mol/L}$). The study of the dynamics of HBD-1 in patients with drug-resistant tuberculosis showed its increase by the second month of treatment from $21.3 \pm 4.8 \mu\text{mol/L}$ (median – $3.7 \mu\text{mol/L}$) to $42.1 \pm 8.2 \mu\text{mol/L}$ (median – $52.7 \mu\text{mol/L}$). **Conclusions.** The spectrum of drug-resistance does not affect the level of Human-beta-defensin-1 in patients with pulmonary tuberculosis. The initial level depends on the pulmonary lesions size, the presence of bacterial excretion and liver function impairment. Treatment of drug-susceptible tuberculosis leads to a significant decrease in Human-beta-defensin-1 by the second month, in contrast to cases of drug-resistant tuberculosis. The dependence of the effectiveness of treatment of drug-resistant tuberculosis on the initial level of Human-beta-defensin-1 was revealed: the lower the level of Human-beta-defensin-1, the higher the treatment effectiveness, which makes it possible to use this parameter as a prognostic marker of the treatment effectiveness.

Key words: tuberculosis, Human-beta-defensin-1, drug-resistance

Introduction. Taking into account the constant expansion of *M. tuberculosis* drug resistance, the study of the host immune response components, which can be used in diagnosis, prediction of tuberculosis course and pathogenetic treatment, is becoming an increasingly urgent issue.

One of these components are cationic

peptides, in particular the β -defensin family. Recent study of Zhu et al. [1] showed high effectiveness of Human-beta-defensin-3 against methicillin-resistant *Staphylococcus aureus* in murine model. The similar study was provided earlier by Maisetta et al. [2] in vitro against multidrug-resistant strains of *aureus*,

Enterococcus faecium, *Pseudomonas aeruginosa*, *Stenotrophomonas maltophilia* and *Acinetobacter baumannii*.

Despite the fact that β -defensins-2, -3 and 4 are not primary in the immune response, do not have a basic level of production and their production is stimulated by β -defensin-1 [3], detailed study of β -defensin-1 role in immune response was not provided until recently. Only in 2019, a study by Wendler et al. [4] showed the model of β -defensin-1 influence on antibiotic-resistant strains of *E. coli*, *P. aeruginosa*, and *C. albicans*, and suggested the possibility of using β -defensin-1 as a component of pathogenetic therapy supporting the host's immunity.

It should be noted that ongoing studies of the activity of β -defensins included the study of their effect on common species of the families *Candida*, *Staphylococcus*, *Escherichia*, but did not include the effect on *M. tuberculosis*, which is nevertheless a complex epidemiological problem for many countries [5]. A detailed study of the effect of various regimens of anti-tuberculosis therapy with the use of first and second line anti-tuberculosis drugs was not carried out.

Therefore, the dynamics of Human-beta-defensin-1 level described in this work under various resistance spectra of *M. tuberculosis* and anti-tuberculosis treatment regimens is a topical study, and the results obtained can be used in the future to improve the diagnosis and treatment of drug-resistant tuberculosis.

The purpose of the study was to compare Human-beta-defensin-1 level in different types of drug-resistance in patients with pulmonary tuberculosis and its dynamics during use of standard and individualized regimens of anti-tuberculosis treatment.

Materials and methods. 100 patients were included in the study and divided into groups: Group 1 – 52 patients with drug-susceptible tuberculosis (TB), Group 2 – 48 patients with drug-resistant tuberculosis (Group 2.1 – mono-resistant tuberculosis (n=15), Group 2.2. – multidrug-resistant tuberculosis (MDR-TB) (n=21), Group 2.3 – extensively drug-resistant tuberculosis (XDR-TB) (n=12)). Human-beta-defensin-1 (HBD-1) level was measured in all the patients at the treatment onset and 2 months later. The patients were also examined according to the current Order of

Ministry of Health of Ukraine which included chest X-ray, sputum smear microscopy, sputum molecular-genetic study, sputum culture on liquid and solid media, blood count, blood biochemistry. Patients were treated with standard and individualized treatment regimens which included during intensive phase: 4 first-line drugs for patients with susceptible tuberculosis; 4 first- and second-line drugs for patients with mono-resistant tuberculosis, 4-5 second-line drugs for patients with MDR-TB and XDR-TB with or without added bedaquiline. Due to treatment interruption or death to the second month of treatment the number of patients changed and was: Group 1 – 43 patients, Group 2.1 – 15 patients, Group 2.2 – 17 patients, Group 2.3 – 10 patients. Statistical data processing was carried out using Statistica 8.0.

Results. Comparison of HBD-1 level in groups with drug-susceptible and drug-resistant tuberculosis at the treatment onset showed no significant difference ($p>0.05$): Group 1 - 20.4 ± 3.6 $\mu\text{mol/L}$, Group 2 - 21.4 ± 4.8 $\mu\text{mol/L}$. However, after 2 months of anti-tuberculosis treatment HBD-1 level was significantly higher in Group 2 (42.1 ± 8.2 $\mu\text{mol/L}$, median – 16,8 $\mu\text{mol/L}$) than in Group 1 (15.9 ± 5.3 $\mu\text{mol/L}$, median – 38.4 $\mu\text{mol/L}$), $p<0.05$ (Fig. 1)

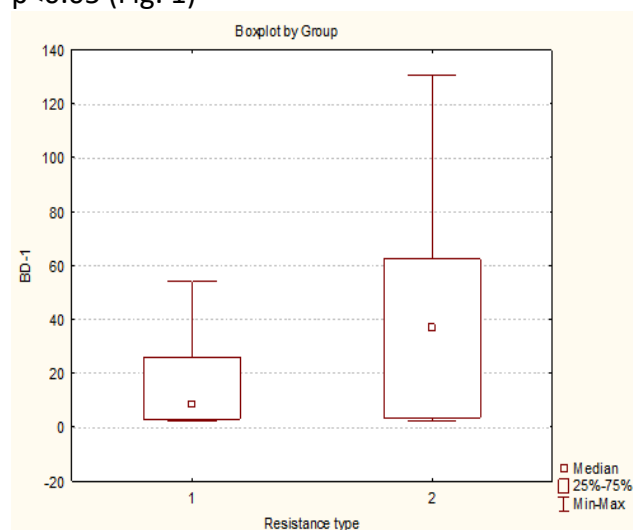


Figure 1. Comparison of Human-beta-defensin-1 level in patients with drug-susceptible (Group 1) and drug-resistant (Group 2) tuberculosis after 2 months of anti-tuberculosis treatment

To study the influence of resistance type on HBD-1 level we compared groups with different types of drug-resistance. There was no significant difference at the treatment onset ($p<0.05$), but

there was a tendency to HBD-1 increase with widening of drug-resistance spectrum. HBD-1 level was: in mono-resistant patients – 9.7 ± 4.7 $\mu\text{mol/L}$, in MDR-TB patients – 17.3 ± 4.3 $\mu\text{mol/L}$, in XDR-TB patients – 32.5 ± 14.0 $\mu\text{mol/L}$. After 2 months of treatment, there was a significant ($p < 0.05$) difference between HBD-1 levels in patients with different types of drug-resistance with its increase in wider resistance spectrum: in mono-resistant TB – 12.6 ± 5.8 $\mu\text{mol/L}$ (median – 12.0 $\mu\text{mol/L}$), in MDR-TB – 38.1 ± 6.9 $\mu\text{mol/L}$ (median – 56.2 $\mu\text{mol/L}$), in XDR-TB – 71.8 ± 28.5 $\mu\text{mol/L}$ (median – 104.8 $\mu\text{mol/L}$) (Fig. 2).

Further study of correlations of HBD-1 and other parameters was provided independently in groups. HBD-1 level did not influence treatment effectiveness in patients with drug-susceptible tuberculosis which can be due to small size of group of patients with non-effective treatment. Despite this we noted that higher HBD-1 level correlated with larger pulmonary lesions ($r = +0.44$, $p < 0.05$) and presence of pulmonary tissue destruction: patients with pulmonary tissue destruction had HBD-1 level 25.7 ± 5.0 $\mu\text{mol/L}$ (median – 23.6 $\mu\text{mol/L}$), patients without pulmonary tissue destruction had HBD-1 level 12.9 ± 4.4 $\mu\text{mol/L}$ (median – 7.1 $\mu\text{mol/L}$), $p < 0.05$ (Fig. 3).

Since HBD-1 is a natural cationic immune peptide, its synthesis also depends on the state of the protein-synthetic function of the liver, which was confirmed by positive correlations between the level of HBD-1 and total protein ($r = +0.66$, $p < 0.05$) and also between the level of HBD-1 and thymol test ($r = +0.45$, $p < 0.05$). The functioning of HBD-1 as an inflammatory agent was confirmed by its positive correlation with such a nonspecific marker of inflammation as ESR ($r = +0.78$, $p < 0.05$).

The study of the dynamics of HBD-1 in patients with drug-resistant tuberculosis showed its increase by the second month of treatment from 21.3 ± 4.8 $\mu\text{mol/L}$ (median – 3.7 $\mu\text{mol/L}$) to 42.1 ± 8.2 $\mu\text{mol/L}$ (median – 52.7 $\mu\text{mol/L}$), $p < 0.05$ (Fig. 4).

Comparison of the HBD-1 level in patients with drug-resistant tuberculosis depending on the effectiveness of the intensive phase of anti-tuberculosis treatment showed that initial HBD-1 was significantly higher in patients who completed the intensive phase of treatment

ineffectively (36.9 ± 11.8 $\mu\text{mol/L}$, median – 30.4 $\mu\text{mol/L}$) than in those who completed it effectively (16.4 ± 4.9 $\mu\text{mol/L}$, median – 3.2 $\mu\text{mol/L}$), $p < 0.05$ (Fig. 5).

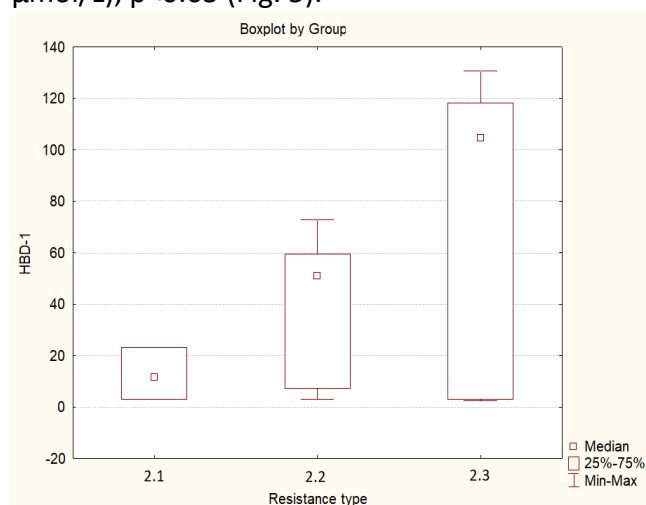


Figure 2. Comparison of Human-beta-defensin-1 level in patients with mono-resistant TB (Group 2.1), MDR-TB (Group 2.2) and XDR-TB (Group 2.3) after 2 months of anti-tuberculosis treatment

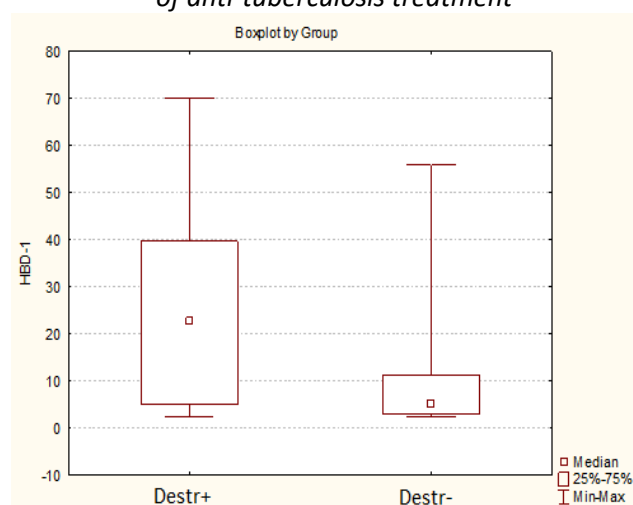


Figure 3. Comparison of Human-beta-defensin-1 level in patients with and without destruction of lung tissue

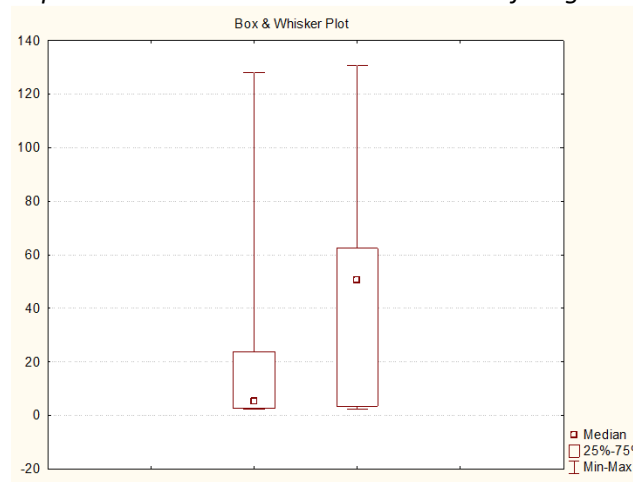


Figure 4. Dynamics of Human-beta-defensin-1 level in patients with drug-resistant tuberculosis

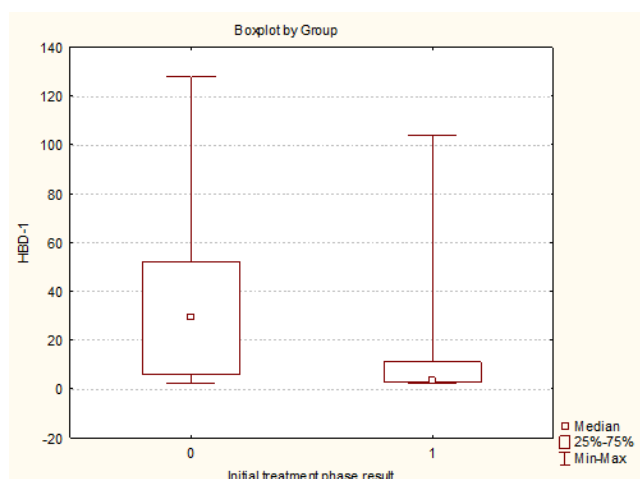


Figure 5. Comparison of Human-beta-defensin-1 level at the treatment onset in patients who completed initial phase of anti-tuberculosis treatment ineffectively (0) and effectively (1)

An increased initial HBD-1 level led to the persistence of a greater bacterial excretion at the 2nd month of treatment ($r = +0.57$). In addition, we found a correlation between an increased HBD-1 and impaired liver function, namely increased ALT ($r = +0.55$, $p < 0.05$) and AST ($r = +0.54$, $p < 0.05$).

It was interesting to compare the effect of different regimens of anti-tuberculosis treatment of MDR-TB and XDR-TB on the HBD-1 level. It was found that in patients who received new anti-tuberculosis treatment regimens with the addition of bedaquiline, the level of HBD-1 at the second month of treatment was significantly lower ($19.1 \pm 13.4 \mu\text{mol/L}$ (median - $12.8 \mu\text{mol/L}$) than in patients who received individualized 20-month courses of treatment without bedaquiline ($45.7 \pm 5.3 \mu\text{mol/L}$ (median - $52.3 \mu\text{mol/L}$), $p < 0.05$ (Fig. 6).

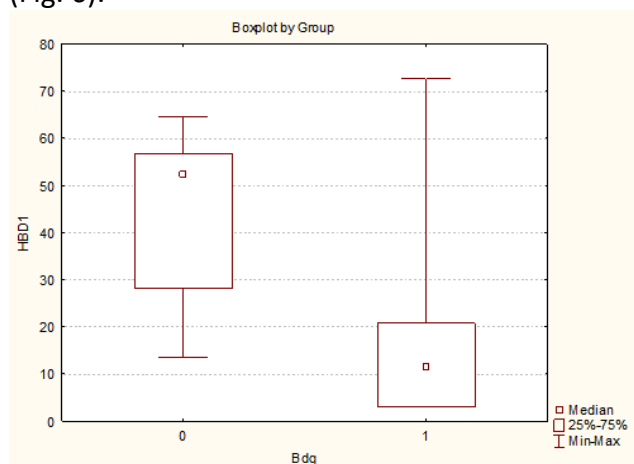


Figure 6. Comparison of Human-beta-defensin-1 level at the 2nd month of treatment in patients with MDR-TB and XDR-TB receiving treatment regimens with (1) and without (0) bedaquiline

At the same time, 100.0% of patients who received treatment regimens with the addition of bedaquiline had sputum conversion by the 2nd month of treatment, while patients treated without bedaquiline had sputum conversion by the 2nd month of treatment only in 73.1% of cases. ($p < 0.05$).

Discussion. The obtained results of the comparison of the dynamics of the HBD-1 levels can be explained by the peculiarities of its production directly in response to the effect of microbial antigens [6]. Thus, at the beginning of treatment, when the antigenic load is high, all patients show increased HBD-1 level. After 2 months of treatment, the bacterial load in drug-susceptible TB is significantly reduced, patients start supportive phase of treatment and the production of HBD-1 also decreases. In drug-resistant tuberculosis, in particular MDR-TB and XDR-TB, a high activity and concentration of *M. tuberculosis* is still preserved at the 2nd month of treatment, which explains the persistence of high HBD-1 level in these patients. This fact is confirmed by the positive correlation of the average strength between the HBD-1 level and the massiveness of bacterial excretion at the 2nd month of treatment. Moreover, many patients with drug-resistant TB have severe intoxication and cachexy, so that the normalization of metabolism, particularly protein exchange, starts to normalize only by the 2nd month of treatment creating favorable conditions for the production of cationic peptides as factors of the immune response. This explains the growth the HBD-1 level in the group of patients with drug-resistant tuberculosis. Thus, in a study by Mao et al. in an animal model, normalization of protein metabolism by the introduction of amino acids and microelements was able to stimulate the production of β -defensin and increase the level of resistance of the host organism to microbial agents [9]. On the other hand, such an increase in HBD-1 levels may also be associated with the hepatotoxic effect of anti-tuberculosis drugs. A recent study by Kaltsa et al. showed a relationship between an increase of HBD-1 level and an increase of liver enzymes in patients with liver cirrhosis [8]. In our study, this hypothesis is confirmed by the positive correlation between the HBD-1 level and the levels of ALT and AST. In a study by Aksoy et al. [7] the same correlation was

observed in patients with Crimean-Congo hemorrhagic fever, but in their study such a correlation was a positive prognostic marker and was observed only in the group of survivors.

The introduction of new treatment regimens for MDR-TB and XDR-TB using bedaquiline makes it possible to accelerate the elimination of *M. tuberculosis*, which is confirmed by a significantly more frequent sputum conversion at the 2nd month of treatment. Therefore, in these patients we see lower level of HBD-1, which indicates a decrease in the severity of inflammatory reactions and a normalization of the immune response.

A promising direction is the study of the possibilities of HBD-1 using as a prognostic marker. In our study, a relationship between an increase of HBD-1 level and an increase of lesion size was found, as well as the formation of destruction of pulmonary tissue, which allows us to consider it as a marker of the severity of tuberculous lesion. In addition, the correlation between HBD-1 level and the massiveness of bacterial excretion at the 2nd month of treatment in patients with drug-resistant tuberculosis, as well as a higher initial level of HBD-1 in patients with an ineffective intensive phase of anti-tuberculosis therapy, allows using it as a prognostic marker of the anti-tuberculosis treatment effectiveness.

Conclusions. The spectrum of drug-resistance does not affect the level of Human-beta-defensin-1 in patients with pulmonary tuberculosis. The initial level depends on the pulmonary lesions size, the presence of bacterial excretion and liver function impairment. Treatment of drug-susceptible tuberculosis leads to a significant decrease in Human-beta-defensin-1 by the second month, in contrast to cases of drug-resistant tuberculosis. The dependence of the effectiveness of treatment of drug-resistant tuberculosis on the initial level of Human-beta-defensin-1 was revealed: the lower the level of Human-beta-defensin-1, the higher the treatment effectiveness, which makes it possible to use this parameter as a prognostic marker of the treatment effectiveness. The use of bedaquiline in treatment regimens for multidrug-resistant and extensively drug-resistant tuberculosis showed a more significant decrease in the level of Human-beta-defensin-1 by the second month of therapy

with sputum conversion in all the patients, which confirms the effectiveness of new regimens for multidrug-resistant tuberculosis and extensively drug-resistant tuberculosis treatment.

References:

1. Zhu C, Bao NR, Chen S, Zhao J-N. The mechanism of human β -defensin 3 in MRSA-induced infection of implant drug-resistant bacteria biofilm in the mouse tibial bone marrow. *Exp Ther Med.* 2017;13(4):1347-52. doi: 10.3892/etm.2017.4112
2. Maisetta G, Batoni G, Esin S, Flowio W, Bottai D, Favilli F, Campa M. Vitro Bactericidal Activity of Human β -Defensin 3 against Multidrug-Resistant Nosocomial Strains. *Antimicrobial Agents and Chemotherapy.* 2006;50(2):806-9. doi: 10.1128/AAC.50.2.806-809.2006
3. Tomalka J, Azodi E, Narra HP, Patel K, O'Neill S, Cardwell C, et al. Beta-defensin 1 plays a role in acute mucosal defense to *Candida albicans*. *J Immunol.* 2015;194(4):1788-1795. doi: 10.4049/jimmunol.1203239
4. Wendler J, Schroeder BO, Ehmann D, Koeninger L, Mailander-Sanchez D, Lemberg C, et al. Proteolytic Degradation of reduced Human Beta Defensin 1 generates a Novel Antibiotic Octapeptide. *Scientific Reports.* 2019;9:3640. doi: 10.1038/s41598-019-40216
5. WHO Global Tuberculosis Report 2019, 297 p. https://www.who.int/tb/publications/global_report/en/
6. Harder J, Meyer-Hoffert U, Teran LM, Schwichtenberg L, Bartels J, Maune S, et al. Mucoïd *Pseudomonas Aeruginosa*, TNF- α , and IL-1 β , but Not IL-6, Induce Human beta-defensin-2 in Respiratory Epithelia. *Am J Respir Cell Mol Biol.* 2000;22(6):714-21. doi: 10.1165/ajrcmb.22.6.4023
7. Aksoy O, Parlak E, Parlak M, Aksoy H. Serum β -Defensin-2 Levels and Their Relationship with the Clinical Course and Prognosis in Patients with Crimean-Congo Hemorrhagic Fever. *Med Princ Pract.* 2016;25(2):163-8. doi: 10.1159/000442177
8. Kaltsa G, Bamias G, Siakavellas SI, Goukos D, Karagiannakis D, Zampeli E, et al. Systemic levels of human β -defensin 1 are elevated in patients with cirrhosis. *Annals of Gastroenterology.* 2016;29:63-70.
9. Mao X, Qi S, Yu B, He J, Yu J, Chen D. Zn(2+) and L-isoleucine Induce the Expressions of Porcine β -defensins in IPEC-J2 Cells. *Mol Biol Rep.* 2013;40(2):1547-52. doi: 10.1007/s11033-012-2200-0

Fridman R.

Ph. D. Student (System Analysis) of the Department of Mathematical Methods of System Analysis, NTUU "Igor Sikorsky KPI", Kyiv, Ukraine, E-mail: ron@mawi.band

A COMPARISON OF DEEP NEURAL NETWORK ARCHITECTURES FOR ARRHYTHMIA CLASSIFICATION

Abstract. *In this paper, we describe our studies that compare different types of deep neural networks for automated arrhythmia type classification using the ECG signal. As a source of data and the evaluation benchmark, we took the Physionet Challenge 2017 dataset. In addition to conventional accuracy metrics of the models, we also evaluated the complexities of the models by the number of trainable parameters, to find an optimal trade-off. As a result, our studies bring an evaluation of contemporary deep neural networks architectures on Atrial fibrillation detection task and propose DenseNet as the most efficient in terms of accuracy and computational efficiency.*

Key words: Arrhythmia, AFib, ECG, Neural Network, CNN

Introduction. Nowadays, the classification of ECG signal for heart disease detection is a well-known problem. However, various new methods arise, so it is still a broad field for research. A growth of attention to this problem significantly increased after the publication of Stanford ML group [1], in which they achieved human-level arrhythmia detection using deep neural network (NN) with residual connections. The novelty of the described method was in applying a state-of-the-art NN topology from computer vision to a significant amount of ECG records with corresponding labeled diagnoses. Another advantage of the proposed approach is that it does not require any feature selection as in conventional machine learning (ML) and takes just a raw signal segment as an input. Such an approach is also called “end-to-end machine learning” [2]. Taking into account the success of the mentioned publication, the research community focused on applying this powerful tool using the data from publicly available sources, for instance, PhysioNet web-site [3]. It contains several databases like MIT-BIH Arrhythmia database [4], MIT-BIH Atrial Fibrillation database [3] and PhysioNet Challenge 2017 [5] which include ECG records with atrial fibrillation and can be used for training and testing of machine learning models. This paper will be structured as follows: firstly, in the next chapter, we will describe publications related to arrhythmia classification via different neural networks. Secondly, we will make an overview of existing

publicly-available arrhythmia datasets describing their advantages and drawbacks. Thirdly, in the fourth chapter, we will provide approaches for data preprocessing for neural networks training and in the fifth chapter will describe their characteristics. Next, in the sixth chapter we present a training configuration that was finally applied. In the subsequent chapter we will provide results obtained in several experiments. Finally, in the eighth chapter we will introduce our conclusions based on conducted experiments considering usage of different neural network topologies for arrhythmia detection.

Purpose of the study. There are quite a lot of studies in the field of automated arrhythmia detection; the vast majority of them are using PhysioNet Challenge 2017 dataset and MIT-BIH arrhythmia database as benchmarks. Given papers may be divided into two major groups differing by their data processing pipeline. First type of pipeline is called a “step-by-step” approach and described in [6-10]. It implies whole ECG preprocessing (including annotation) and “manual” feature extraction (mean, std, median, kurtosis, skew, HRV features, wavelet features, features based on lengths of the PQ, ST segments etc.) before classification. The second one is “end-to-end” approach; it implies that the model receives an input signal and produces a prediction without any intermediate steps. The most significant research in this field is previously mentioned in Stanford ML group publication [1]. It is based on a large non-public dataset collected

using iRhythm ECG patch. However, there are also plenty of papers that describe applications of convolutional neural networks on other datasets [11-14], and publications produced by participants of the PhysioNet Challenge [15-18] which showed near the state of the art performance.

Despite the importance of a topic of atrial fibrillation and increased number of discussions after Stanford publication and a new Apple Watch feature release, there is still no unified benchmark for cardiological models (particularly for arrhythmia detection). For instance, the computer vision field has a well-known ImageNet dataset [19], provided by ILSVRC challenge, which is used for testing the performance of multiclass image classification. However, there are three most-used datasets (MIT-BIH Arrhythmia, MIT-BIH AF, PhysioNet challenge2017) from PhysioNet platform that is mostly mentioned in papers dedicated to AF detection tasks. Mentioned databases differ from each other by the number of classes, amount of records and ECG leads they were collected from. Detailed Description with empathized pros and cons of each dataset will be provided further in the chapter.

Materials and methods. The MIT-BIH Arrhythmia Database was the first publicly available standardized database that can be used for cardiac dynamics research and performance evaluation of automatic arrhythmia detectors. It was collected during 1975-1980 at Boston's Beth Israel Hospital in collaboration with MIT on 25 male subjects aged 32 to 89 years and 22 female subjects aged 23 to 89 years. A database contains 48 half-hour records recorded from two chest leads (modified limb lead II and modified lead V1). For analysis, preferably first of two recorded leads, since QRS complexes on it have a normal shape. A big advantage of the given dataset is that it has an annotation of each beat (normal beats(N), premature ventricular contractions(V), supraventricular premature beats (S), or a fusion of ventricular and normal beats (F)). At the same time, ECG intervals have annotations of the corresponding rhythm type (Atrial bigeminy, Atrial fibrillation, Atrial flutter, Ventricular bigeminy, 2 heart block, Idioventricular rhythm, Normal Sinus rhythm, Nodal (A-V junctional) rhythm, Paced rhythm, Pre-excitation (WPW), Sinus bradycardia,

Supraventricular tachyarrhythmia, Ventricular trigeminy, Ventricular trigeminy, Ventricular tachycardia). However, like in most medical datasets, both classes of beat types and rhythm types are very unbalanced and underrepresented; this means that records are hardly suitable for training arrhythmia detectors.

MIT-BIH Atrial Fibrillation Database (AFDB) is also one of the datasets collected by Boston's Beth Israel Hospital and MIT. It is quite similar to MIT-BIH AFDB since ECG records were made from the same chest leads (lead II, lead V1). However, there are only 25 ten-hours records with rhythm annotation, whereas 23 of them also contain raw signal. As its title suggests, database records contain atrial fibrillation episodes, in addition, atrial flutter, AV junctional rhythm and normal sinus rhythm are also available. Although a database has a limited number of records, they are quite long and keeping in mind a principle of patient-independent testing, can be sampled to train machine learning models for arrhythmia detection.

PhysioNet/Computing in Cardiology (CinC) challenge 2017 goal was to perform the best classification performance of ECGs recorded on portable single-channel AliveCorec© devices. The Entire dataset contains 12,186 labelled training records and 300 validation records (labels were hidden during the challenge and used for leaderboard evaluation). All mentioned records are 9-61 seconds long annotated in one out of four labels (normal sinus rhythm, atrial fibrillation, alternative rhythm, and too noisy to consider it an ECG). Despite the fact that this dataset provides a quite big amount of labelled ECG records, there are a few disadvantages to keep in mind while working with it. First, devices that were used for recording do not require specific electrode placement and accept both LA-RA and RA-LA for the lead I as shown on Image 1. So, about half of the records are inverted in terms of voltage and have to be normalized for further processing. Second, initial dataset labelling had some inaccuracies, since it was made by a single practitioner. This issue has not gone undetected during the challenge, so in the latest update of the dataset, the most untrusted records were revised and relabeled. After evaluating the pros and cons of described datasets, we chose PhysioNet

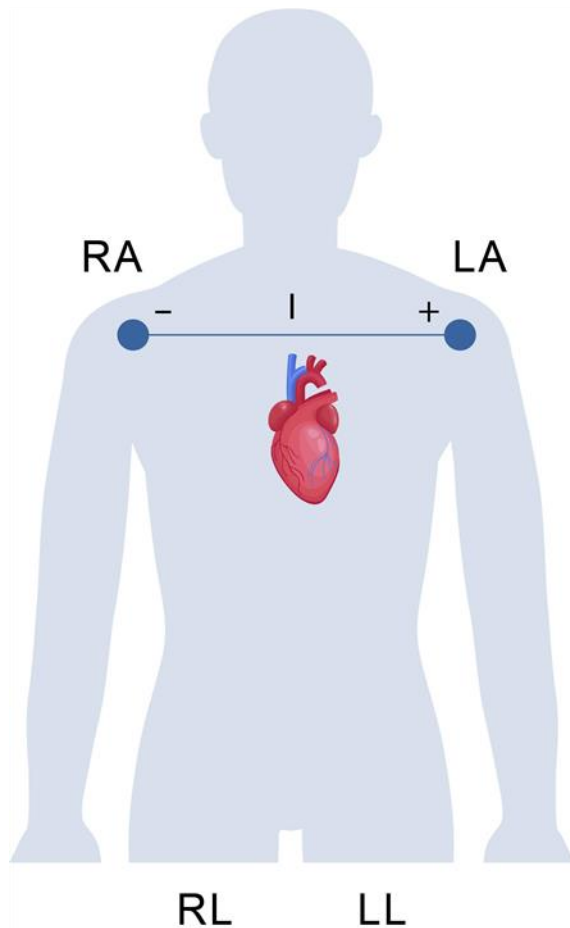
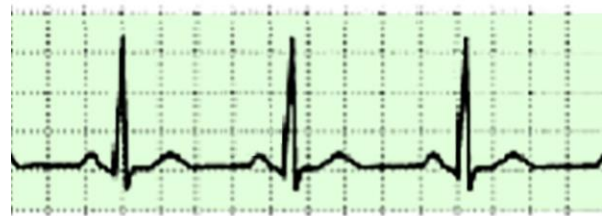


Fig. 1. An electrode placement schema for I ECG lead recording

challenge 2017 dataset for further research. For initial data preprocessing, we used a FIR filter [20] with a cutoff range from 3 Hz to 50 Hz to remove power line and baseline noise. Also, the amplitude of all samples was scaled in the range [0, 1]. As mentioned in chapter 3, the given dataset has an issue with the inverted signal, because of a specific type of ECG recorder. To eliminate this problem and fetch all provided samples, we applied a beat template matching method described by Goodelov [21]. Template matching approach requires signal annotation; thus, Pan-Tompkins [22] algorithm was used. As far as the “noisy” class was underrepresented with only 46 records, it was removed from the analysis. We also experimented with different lengths of dataset samples by taking 15, 30, 45 and 60 seconds of the initial record. If the initial record was long enough to contain several fragments of a certain length, we used them to extend the dataset by sampling multiple samples without overlap from the single record. We will call such dataset configuration as extended. In another

Normal Sinus Rhythm



Atrial Fibrillation



Fig. 2: Normal Sinus Rhythm in comparison with AtrialFibrillation

case, we just took the first required seconds and cut off the remaining part. Such a dataset we will call simple. For the records smaller than required length symmetric zero-padding was applied.

Rhythm abnormalities are visually well recognizable on the ECG signal as we can see on Image 2. In particular, atrial fibrillation is characterized by absence of P-wave or appearance of the specific f-wave on the QT interval on the standard lead I. Therefore, as was proved before in [23], state of the art approaches from the computer vision, that are based on convolutional neural networks (CNNs), also can be used for mentioned task exploiting 1D convolution operation and show competitive results when compared to conventional feature-based methods. In our research, we decided to test all neural network-based approaches starting from simple multilayer perceptron (MLP) to complex topologies like ResNet, DenseNet and combination of CNN and LSTM. Global Average Pooling was used in CNN models before a softmax layer to reduce dimensionality and have an ability to apply CAM approach [24] for construction of attention maps.

To have a baseline, we decided to take MLP as a predecessor of contemporary neural network-based algorithms. It's known that this method has restrictions related to dramatic increase of computational complexity for big input samples. Taking into account the size of the training set

(approximately 8000 records), a sampling rate of records which is 300 Hz, and length up to 60 seconds, the number of hyperparameters to tune will be too high. To tackle this problem we decided to apply some tricks like downsampling or splitting long ECG fragments to shorter ones, which provided more training data and decreased the complexity of the model. A model itself composed of five layers with 450, 300, 100, 64 (fully-connected), 3 (softmax) nodes, ReLU activation functions [25], and Dropouts [26] with rate 0.5. The amount of nodes for each layer and remaining hyperparameters values were selected based on cross validation.

Convolutional Neural Network is a family of neural networks that uses learned filters to match certain templates in the input data. In terms of image processing, the mentioned square-shaped filter moves vertically and horizontally with certain steps. However, in case of ECG, the data is one-dimensional, accordingly, mentioned filters will also have a single dimension and move only along a time axis. For our studies, we decided to try a simple model with five layers which in turn comprised of 1D convolution, Batch Normalization [27], ReLU as activation, max pooling and dropout with rate 0.5. Kernel sizes varied starting from 12 on the initial layers to 6 on the last one, at the same time, stride were selected in range from 8 to 4.

The reason we decided to apply such architecture is to test the performance of long-short-term memory (LSTM) networks [28], which are highly effective in perceiving temporal dependencies in the data. However, LSTM units are quite computationally expensive, taking into account the size of the ECG segments (i.e. 30 seconds \times 500 Hz = 15000 input points). Adding several convolutional layers will solve this issue by reducing the dimensionality and additionally will provide better data representation for LSTM layers. To test this hypothesis we took previously described simple CNN and added a LSTM layer with 100 nodes and a fully connected layer with 65 nodes on top of it before a softmax layer. Given hyperparameters (amount of nodes in the Dense and LSTM layers) were chosen to reach the optimal performance of the model.

ResNet is a specific architecture of deep convolutional neural networks that learns the

residual representation functions instead of direct representation. It represents shortcut (skip) connections that fit an input from the previous layer to the next layer with no changes of the input. Stacking these blocks allows building deeper networks without the occurrence of the vanishing/exploding gradients problems. Initially the given approach showed its advantages on image classification tasks by winning ILSVRC 2015 and MS COCO 2015 in both detection and segmentation. Later, Stanford ML group introduced a study [1] where they trained 34 layer CNN with skip connections on a large dataset of 64,121 ECG records from 29,163 patients. Obtained model outperformed average cardiologist in the classification of 14 different types of heart rhythms disorders. Given paper points to the conclusion that deep CNNs with residual connections are promising techniques for ECG signal classification with different morphology.

DenseNet (densely connected convolutional network) [29] is a topology that shows the state of the art performance in image classification tasks (CIFAR, SVHN, ImageNet) using fewer parameters compared to its closest contender ResNet. Given CNN architecture composed of densely connected blocks (dense blocks). In these blocks, each subsequent layer receives all output feature maps of previous layers, so the number of trainable parameters compared to conventional convolutional models. Such structure gives direct access to the gradient from the loss, which in its turn prevents gradient vanishing/explosion. A major feature of Dense block is that it has the following structure:

- Batch Normalization
- ReLU activation
- Convolution

In which pre-activation happens since batch normalization and activation precede a convolution.

Instead of summing residuals as in ResNet, DenseNet concatenates output feature maps. With no doubts, it's inefficient to concatenate tensors with different sizes. Therefore, all dense blocks have the same feature map size. However, dimensionality compression is essential for CNNs; for these purposes, transition layers are used. They contain Batch Normalization, 1x1

convolution and average pooling. There Are suspicious regarding the complexity of the model because concatenation of feature maps from all layers might lead to an extremely high number of parameters. Fortunately, DenseNet has quite narrow layers with up to 32 feature maps, as recommended by authors.

All NN models were implemented on Keras framework[30] (with the TensorFlow backend [31]). Each model was trained during 80 epochs using Adam optimizer with adjustable learning rate and cross-entropy as an optimization loss function. The initial dataset was divided on training, validation and testing split in proportion 70% / 15% / 15% accordingly. To prevent subject overfitting, samples with required length were fragmented before the train/test split.

Results. Given dataset is quite specific and has its limitations, like severe class imbalance. For this reason, we decided to experiment not only with neural networks types and configurations but also with the formation of classes merging or not using them in particular training experiments. Conducting described experiments, we observed interesting results that will be described further in this section. According to 2017PhysioNet Challenge, average F1-score was used to evaluate the performance of participants, so we decided to follow the same rule for evaluation of our models. Firstly, we trained MLP to have a baseline for our further experiments. To train MLP, we had to overcome a curse of dimensionality, so the sampling rate was reduced from 300 Hz to 30 Hz Fourier method [32]. As expected, MLP tended to overfit and showed the worst performance compared to other models. Next, we decided to build a simple four-layer CNN with filters of bigger size and stride to provide a sufficient down-sampling before global average pooling and softmax activation. A global average pooling was used in most experiments to reduce a total number of parameters in the model and to have an ability of model interpretation using CAM (class activation map) approach [24]. As shown on the table, the simple model performed better than MLP (baseline), but still with low accuracy. Next, we attached a LSTM layer with 64 blocks between the simple model that was described earlier and a fully connected layer with 64 neurons that precedes a softmax activation. This configuration

performed slightly better than the previous model, but still poor classification accuracy. Our Further steps were to try state-of-the-art (SOTA) topologies like ResNet and DenseNet to solve the given classification task. First, we decided to train ResNet as an earlier version CNN with indirect connections. A model contained five subsequently connected residual blocks with global average pooling on top before the softmax layer. Such topology performed much better and showed a result that is quite close to the top of the leaderboard in the PhysioNet/Computing in Cardiology Challenge 2017. Finally, we trained a DenseNet which contained five dense blocks and growth rate 12. It showed the best results with F1-score 0.834 and accuracy. All results for both simple (S) and extended (E) test datasets are shown in Table 1.

Besides classification performance, model complexity is also an important characteristic to analyze. Since we experimented with different types of NN, correspondingly, their complexities also varied. The number of parameters for each model is shown in Table 2. As we can see, the simplest model, in terms of the number of trained parameters, is DenseNet, and the most complex model is ResNet. Taking into account both accuracy and complexity metrics, we selected a DenseNet configuration as far as it is both the most accurate and the most light-weight model for solving given classification problems.

Conclusion. In this work, we trained various deep neural network models starting from simple multilayer perceptron to SOTA topologies like ResNet and DenseNet to classify ECG fragments on Normal Sinus rhythm, AFib rhythm and Other rhythms on different dataset configurations. The best test results were obtained on DenseNet using simple 45-second signal fragments. It is worth mentioning that ResNet showed relatively close performance. However, DenseNet has one significant advantage, thanks to its structural characteristics, it has significantly fewer parameters, so can be considered as more computationally efficient. Furthermore, the high efficiency of such algorithms will allow their integration directly into the stationary cardiographs and even into the wearable devices, which would bring the diagnostics of arrhythmias on the next level. Moreover, this work covers

Table 1.

F1-score of trained NN models

Preprocessing	Window size							
	15		30		45		60	
	S	E	S	E	S	E	S	E
MLP	0.2555	0.2590	0.2520	0.2492	0.2520	0.2487	0.2520	0.2539
CNN	0.5574	0.6202	0.6095	0.6414	0.6138	0.6456	0.5963	0.5991
CNN+LSTM	0.5636	0.6477	0.6244	0.6649	0.6491	0.6511	0.6508	0.6349
ResNet	0.7314	0.7905	0.8090	0.8125	0.8252	0.8254	0.8226	0.81168
DenseNet	0.7491	0.8008	0.8206	0.8111	0.8341	0.8163	0.8221	0.8221

Table 2.

Number of trainable parameters in different NNmodels

	Window size			
	15	30	45	60
MLP	379509	575709	782709	978909
CNN	315907	315907	315907	315907
CNN+ LSTM	353091	353091	353091	353091
ResNet	1065347	1065347	1065347	1065347
DenseNet	186364	186364	186364	186364

most of the novel deep learning architectures and defines a new baseline starting point for further research in Atrial fibrillation detection based on the ECG signal.

References

1. Awni Hannun, Pranav Rajpurkar, Masoumeh Haghpanahi, Geoffrey H. Ti-son, Codie Bourn, Mintu Turakhia, and Andrew Y. Ng. *Cardiologist-level arrhythmia detection and classification in ambulatory electrocardiograms using a deep neural network*. *Nature Medicine*, 25, 01 2019.
2. Ilya Sutskever, Oriol Vinyals, and Quoc V Le. *Sequence to sequence learning with neural networks*. In Z. Ghahramani, M. Welling, C. Cortes, N. D. Lawrence, and K. Q. Weinberger, editors, *Advances in Neural Information Processing Systems* 27, pages 3104–3112. Curran Associates, Inc., 2014.
3. A. L. Goldberger, L. A. N. Amaral, L. Glass, J.

M. Hausdorff, P. Ch.Ivanov, R. G. Mark, J. E. Mietus, G. B. Moody, C.-K. Peng, and H. E. Stanley. *PhysioBank, PhysioToolkit, and PhysioNet: Components of a new research resource for complex physiologic signals*. *Circulation*, 101(23):e215–e220, 2000 (June 13). *Circulation Electronic Pages*: <http://circ.ahajournals.org/content/101/23/e215.full> PMID:1085218; doi:10.1161/01.CIR.101.23.e215.

4. G. B. Moody and R. D. Davies Mark. *The impact of the mit-bih arrhythmia database*. *IEEE Engineering in Medicine and Biology Magazine*, 20:45–50, 2001.

5. Gari D. Clifford, Changchun Liu, Benjamin Moody, Li wei H. Lehman, Ikaro Silva, Qiao Li, Alistair Edward William Johnson, and Roger G. Mark. *Af classification from a short single lead ecg recording: The Physionet/computing in*

cardiology challenge 2017.2017 Computing inCardiology (CinC), pages 1–4, 2017.

6. F. Alonso-Atienza, E. Morgado, L. Fernández-Martínez, A. García-Alberola, and J. L. Rojo-Álvarez. Detection of life-threatening arrhythmias using feature selection and support vector machines. *IEEETransactions on Biomedical Engineering*, 61(3):832–840, March 2014.

7. Kemal Polat and Salih Güneş. Detection of ecg arrhythmia using a differential expert system approach based on principal component analysis and least square support vector machine. *Applied Mathematics andComputation*, 186(1):898 – 906, 2007.

8. Juan Ródenas García, Manuel Garcia, Raúl Alcaraz, and Jose Rieta. Wavelet entropy automatically detects episodes of atrial fibrillation from single-lead electrocardiograms. *Entropy*, 17:6179–6199, 09 2015.

9. Mjaye Mazwi, Sebastian Goodfellow, Andrew Goodwin, Robert Greer, Peter C. Laussen, and Danny Eytan. Atrial fibrillation classification using step-by-step machine learning. *Biomedical Physics EngineeringExpress*, 4, 04 2018.

10. Deeptankar Demazumder, Douglas Lake, Alan Cheng, Travis Moss, Eliseo Guallar, Robert Weiss, Steven Jones, Gordon F Tomaselli, and Joseph Moorman. Dynamic analysis of cardiac rhythms for discriminating atrial fibrillation from lethal ventricular arrhythmias. *Circulation. Arrhythmia and electrophysiology*, 6, 05 2013.

11. U. Rajendra Acharya, Hamido Fujita, Oh Shu Lih, Yuki Hagiwara, Jen Hong Tan, and Muhammad Adam. Automated detection of arrhythmias using different intervals of tachycardia ecg segments with convolutional neural network. *Information Sciences*, 405:81 – 90, 2017.

12. U. Rajendra Acharya, Hamido Fujita, Oh Shu Lih, Yuki Hagiwara, Jen Hong Tan, and Muhammad Adam. Automated detection of arrhythmias using different intervals of tachycardia ecg segments with convolutional neural network. *Information Sciences*, 405:81 – 90, 2017.

13. B. Pourbabae, M. J. Roshtkhari, and K. Khorasani. Feature leaning with deep convolutional neural networks for screening patients with paroxysmal atrial fibrillation. In 2016

International Joint Conference on Neural Networks (IJCNN), pages 5057–5064, July 2016.

14. Rishikesan Kamaleswaran, Ruhi Mahajan, and Oguz Akbilgic. A robust deep convolutional neural network for the classification of abnormal cardiac rhythm using varying length single lead electrocardiogram. *Physiological Measurement*, 39, 01 2018.

15. Rishikesan Kamaleswaran, Ruhi Mahajan, and oguz akbilgic. A robust deep convolutional neural network for the classification of abnormal cardiac rhythm using varying length single lead electrocardiogram. *Physiological Measurement*, 39, 01 2018.

16. Martin Zihlmann, Dmytro Perekrestenko, and Michael Tschannen. Convolutional recurrent neural networks for electrocardiogram classification. 10 2017.

17. Jonathan Rubin, Saman Parvaneh, Asif Rahman, Bryan Conroy, and Saeed Babaeizadeh. Densely connected convolutional networks for detection of atrial fibrillation from short single-lead ecg recordings. *Journal of Electrocardiology*, 51, 08 2018.

18. Philip Warrick and Masun Nabhan Homs. Cardiac arrhythmia detection from ecg combining convolutional and long short-term memory networks. 09 2017.

19. J. Deng, W. Dong, R. Socher, L.-J. Li, K. Li, and L. Fei-Fei. ImageNet: A Large-Scale Hierarchical Image Database. In *CVPR09*, 2009.

20. K. S. Kumar, B. Yazdanpanah, and P. R. Kumar. Removal of noise from electrocardiogram using digital fir and iir filters with various methods. In 2015 International Conference on Communications and Signal Processing (ICCSP), pages 0157–0162, April 2015.

21. Sebastian Goodfellow, Andrew Goodwin, Danny Eytan, Robert Greer, Mjaye Mazwi, and Peter Laussen. Towards understanding ecg rhythms classification using convolutional neural networks and attention mappings. 08 2018.

22. J. Pan and W. J. Tompkins. A real-time qrs detection algorithm. *IEEETransactions on Biomedical Engineering*, BME-32(3):230–236, March 1985.

23. Alex Krizhevsky, Ilya Sutskever, and Geoffrey E. Hinton. Imagenet clas-sification with deep convolutional neural networks. *Neural InformationProcessing Systems*, 25, 01 2012.

24. Bolei Zhou, Aditya Khosla, Àgata Lapedriza, Aude Oliva, and AntonioTorralba. Learning deep features for discriminative localization. 12 2015.
25. Xavier Glorot, Antoine Bordes, and Yoshua Bengio. Deep sparse rectifier neural networks. In Geoffrey Gordon, David Dunson, and Miroslav Dudík, editors, *Proceedings of the Fourteenth International Conference on Artificial Intelligence and Statistics*, volume 15 of *Proceedings of Machine Learning Research*, pages 315–323, Fort Lauderdale, FL, USA, 11–13 Apr 2011. PMLR.
26. Nitish Srivastava, Geoffrey E. Hinton, Alex Krizhevsky, Ilya Sutskever, and Ruslan R. Salakhutdinov. Dropout: a simple way to prevent neural networks from overfitting. *Journal of Machine Learning Research*, 15:1929–1958, 2014.
27. Sergey Ioffe and Christian Szegedy. Batch normalization: Accelerating Deep network training by reducing internal covariate shift. 02 2015.
28. F. A. Gers, J. Schmidhuber, and F. Cummins. Learning to forget: continual prediction with lstm. In 1999 Ninth International Conference on Artificial Neural Networks ICANN 99. (Conf. Publ. No. 470), volume 2, pages 850–855 vol.2, Sep. 1999.
29. Gao Huang, Zhuang Liu, Laurens van der Maaten, and Kilian Q. Weinberger. Densely connected convolutional networks. In *The IEEE Conference on Computer Vision and Pattern Recognition (CVPR)*, July 2017.
30. François Chollet et al. Keras. <https://github.com/fchollet/keras>, 2015.
31. Martín Abadi, Ashish Agarwal, Paul Barham, Eugene Brevdo, Zhifeng Chen, Craig Citro, Greg S. Corrado, Andy Davis, Jeffrey Dean, Matthieu Devin, Sanjay Ghemawat, Ian Goodfellow, Andrew Harp, Geoffrey Irving, Michael Isard, Yangqing Jia, Rafal Jozefowicz, Lukasz Kaiser, Manjunath Kudlur, Josh Levenberg, Dan Mané, Rajat Monga, Sherry Moore, Derek Murray, Chris Olah, Mike Schuster, Jonathon Shlens, Benoit Steiner, Ilya Sutskever, Kunal Talwar, Paul Tucker, Vincent Vanhoucke, Vijay Vasudevan, Fernanda Viégas, Oriol Vinyals, Pete Warden, Martin Wattenberg, Martin Wicke, Yuan Yu, and Xiaoqiang Zheng. TensorFlow: Large-scale machine learning on heterogeneous systems, 2015. Software available from [tensorflow.org](https://www.tensorflow.org).
32. W. G. Hawkins. Fourier transform resampling: theory and application [medical imaging]. In 1996 IEEE Nuclear Science Symposium. Conference Record, volume 3, pages 1491–1495 vol.3, Nov 1996.

Sahan V.

Ph. D. Student (System Analysis) of the Department of Mathematical Methods of System Analysis, NTUU "Igor Sikorsky KPI", Kyiv, Ukraine, E-mail: vitalii@mawi.band

TOWARDS THE ECG-BASED BIOMARKERS OF HUMAN AGING

Abstract. The rates of aging may vary substantially among the different individuals and population groups. Multiple attempts have been made to develop the biologically- relevant biomarkers of human aging using molecular and imaging data. Electrocardiogram (ECG) is one of the most accessible clinical tests used by physicians to examine the health state of patients. Wearable devices that can measure ECG on demand (often on the form of wristbands or smartwatches like Apple Watch or Mawi Band) or continuously (chest patches like iRhythm or Qardio) have gained a lot of popularity in recent years offering an accessible and affordable alternative to other biomedical tests. This increased availability of data provides unprecedented opportunities not only for medical diagnosis but also for aging research and longevity biotechnology. This work explores the possibility of using an electrocardiogram (ECG) and derived features as a biomarker of aging. Our contribution is twofold. Firstly, we collected a comprehensive dataset from two different sources: 24-hours Holter cardiograph recordings of around 1000 individuals and 5-minute wearable cardiograph recordings of 500 individuals. Secondly, we identified several potential biomarkers of aging including fiducial features of raw ECG signal (QT segment variability), heart rate variability characteristics (time-domain measures including standard deviation of NN intervals (SDNN) and such frequency-domain measures as powers of the low-frequency (LF) and high-frequency (HF) bands) that show high correlations with chronological age. Further validation has demonstrated that most of these features remain significant both for long-term recordings from medical cardiographs and short-term recordings from wearable devices. These results suggest the emerging potential of combining wearable sensors and machine learning technologies for continuous health risk monitoring with real-time feedback to life and health insurance, healthcare, and wellness providers.

Key words: aging, ECG, biomarker

Introduction. Numerous physiological parameters show significant correlation with an individual's age. Recently research in this direction had been driven by experiments with DNA methylation [1], gene expression [2], plasma proteome [3] and similar data, which is relatively difficult to obtain at the moment (both from the pricing and processual point of view). In this study we aim to develop a set of biomarkers of aging from a more accessible source of data. We have chosen the humans heart as this source, because ECG collecting is a non-invasive and relatively cheap procedure. Furthermore, with growing popularity of pulse trackers and wearable ECG monitors it can be very accessible for the broader masses. The obtained biomarkers can be used for several purposes, in particular, evaluation of aging dynamics in different populations, clinical trials, drug development and testing.

There are several related works showing potential of the use of ECG as a source of biomarker of aging [4], [5]). Most of them show, that heart rate variability (HRV) related parameters correlate with the age at most, namely SDNN, RMSSD, pNN50, LF, HF (low frequency and high frequency) and others. Minority of the works show correlation of fiducial ECG features like QT interval variability [7], ST wave depression[8] and others with chronological

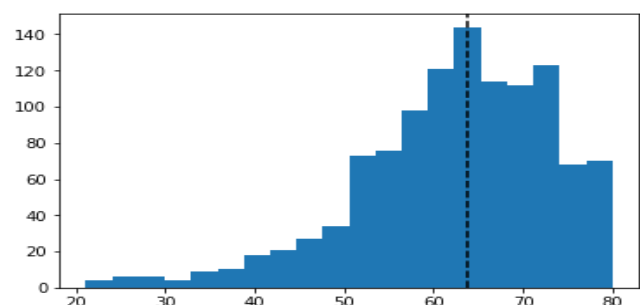


Fig. 1: Ages distribution in the dataset

age. There are also studies with promising approaches based on information theory approaches, in particular, entropy or detrended fluctuation analysis (DFA), see [6], extracted from RR-intervals time series.

Numerous physiological parameters show significant correlation with an individual's age. Recently research in this direction had been driven by experiments with DNA methylation [1], gene expression [2], plasma proteome [3] and similar data, which is relatively difficult to obtain at the moment (both from the pricing and processual point of view). In this study we aim to develop a set of biomarkers of aging from a more accessible source of data. We have chosen the human heart as this source, because ECG collecting is a non-invasive and relatively cheap procedure. Furthermore, with the growing popularity of pulse trackers and wearable ECG monitors it can be very accessible for the broader masses. The obtained biomarkers can be used for several purposes, in particular, evaluation of aging dynamics in different populations, clinical trials, drug development and testing.

There are several related works showing potential of the use of ECG as a source of biomarker of aging (see [4], [5]). Most of them show that heart rate variability (HRV) related parameters correlate with the age at most, namely SDNN, RMSSD, pNN50, LF, HF (low frequency and high frequency) and others. Minority of the works show correlation of fiducial ECG features like QT interval variability [7], ST wave depression [8] and others with chronological age. There are also studies with promising approaches based on information theory approaches, in particular, entropy or detrended fluctuation analysis (DFA) (see [6]), extracted from RR-intervals time series.

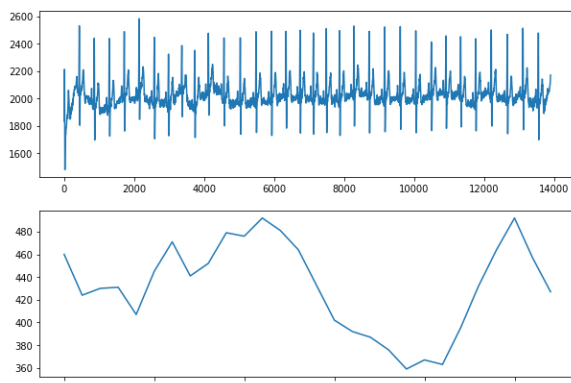


Fig. 2: Example of ECG and corresponding RR intervals lengths

Nevertheless, most of them do not have enough participants in the practical experiments or use the long-term ECG recordings that are not always accessible. On the contrary, in this work we have gathered a large scale dataset of more than 1000 individuals and we show several experiments exploiting both long-term and short-term recordings measured with different frequencies.

This paper is organized as follows: first, we will describe a dataset used for analysis, individuals in it, extracted ECG features and how they are correlated with a chronological age. Next, we will describe the modeling experiment, validation scheme and the numerical results. Then we will discuss the obtained results and, at the end, we will show the room for practical use of this work and further improvements.

Materials and methods. In this section we describe the dataset and methods we used in this study, its origin, statistical properties alongside with the ECG features and their correlations with the age that were extracted from the raw ECG signal.

Our study population initially consists of people who measured their cardiograms based on the doctor's prescription, or for the purposes of preventive diagnostics in one of the medical institutions in Kyiv, Ukraine. The ECG recordings were measured using standard Holter cardiograph during 24 hours, while the patients under study were acting like they're used to.

Since doctors prescribe Holter monitoring only to the aging groups that are in the potential risk of different heart diseases, the initial dataset consists of the individuals, whose chronological age is biased towards higher values. See Figure 1 for the detailed histogram of the initial dataset.

Also, we needed to filter our dataset from the individuals with heart pathologies that appear with the age. We do this to avoid a situation, when the extracted variables from the ECG signal do not correlate with the actual individual's age itself, but with the diseases. This way our models will estimate not only the biological age of the heart, but the presence or absence of some particular diseases, namely suffered heart strokes, various arrhythmia types, ischemia and others.

The raw ECG signal was obtained from Holter cardio-graphs that have 200Hz sampling rate and

were measured during 24 hours. After that we have extracted the features, described in detail in the table 1 further. First, there is a group of variables, derived on the basis of the time domain analysis of the RR intervals:

1. SDNN-Standard deviation of all normal RR intervals. Considered to reflect the total effect of autonomic regulation of blood circulation.
2. RMMSD-The square root of the sum of differences in a series of cardio intervals. Considered to reflect activity of parasympathetic link of autonomic regulation.
3. Heart rate is the speed of the heartbeat measured by the number of contractions (beats) of the heart per minute (bpm).
4. pNN50 - The proportion of pairs of successive NNs that differ by more than 50 ms divided by the total number of NNs. It is an indicator of the degree of predominance of the parasympathetic link of regulation over the sympathetic.
5. MxDMn - The difference between the maximum and minimum values of cardio intervals. It was considered to represent the maximum amplitude of regulatory influences.
6. SI-Stress-index developed by Professor Roman M. Baevsky. Represents the degree of tension of regulatory systems (the degree of predominance of the activity of central regulatory mechanisms over autonomous), see [13] for details.

Then, there are features based on the frequency domain analysis:

1. Total power - The total power of the HRV spectrum. Considered to represent the total absolute level of activity of regulatory systems.
2. HF power - Power spectra in high frequency range (0.15 - 0.40Hz). Shows the relative level of parasympathetic regulation activity.
3. LF power - Power spectra in low frequency range (0.04 - 0.15Hz). Shows the relative level of activity of the sympathetic level of regulation.
4. VLF power - Power spectra in very low frequency range (Less than 0.04Hz).
5. LF/HF - LF to HF ratio. Considered to characterize the Sympathetic to Parasympathetic Autonomic Balance and reflect relative activity of the subcortical sympathetic nerve center.
6. LFnu - Normalized LF value calculated as

$LF/(HF+LF)$

7. HFnu - Normalized HF value calculated as $HF/(HF+LF)$

Finally, there is a group of other features as well:

1. CC0 - The number of shifts of the autocorrelation function until the value of the correlation coefficient is less than zero. Represents the degree of activity of the central regulation loop.
2. CC1 - The value of the first coefficient of the autocorrelation function. Considered to represent the degree of activity of the autonomous regulation loop.
3. SD1 - RR-interval Poincare plot index - the standard deviation of the distance of each point from the $y=x$ axis. Specifies the RR-interval Poincare plot ellipses width. SD1 measures short-term HRV in ms.
4. SD2 - RR-interval Poincare plot index - the standard deviation of each point from the $y=x+(\text{average RR interval})$. Specifies the RR-interval Poincare plot ellipses length. SD2 measures short- and long-term HRV in ms and correlates with LF power.
5. SD1/SD2 - SD1 to SD2 ratio. Measures the unpredictability of the RR time series, may be used to measure autonomic balance. SD1/SD2 is correlated with the LF/HF ratio.
6. Artefact amount - Amount of artefacts detected in the record.

It's also important to mention that no specific data was available related to patients' mortality. Of course, additional clinical and biological data will be needed in the future experiments for more accurate heart biomarkers development.

In this section, we show how based on the extracted features from the raw 24-hours ECGs we build experiments on the prediction of the individuals' age in different settings: from the long-term or short-term recordings. Then, we describe algorithms we used for prediction and evaluation schemes.

Since we were extracting the features both from the full 24-hours recording and 5-minutes subsequences, we're interested in three realistic experiments. First one is related to the situation, when we want to predict individuals' age based on the whole 24 hours of Holter monitoring. In this case, we can use all the extracted features

Table 1

This is my one big table

Feature	24 hours	Mean short terms	Std short terms
CC!	-0.25	-0.38	0.12
HystAmo	0.15	0.10	0.14
HystMo	0.15	0.13	-0.06
MxDMn	0.03	0.14	0.08
PARS	0.06	0.35	0.07
SD1/SD2	0.22	0.03	0.03
Stress Index	0.04	0.08	0.09
Artefact	0.09	0.10	0.03
HF power	0.21	0.22	0.15
HF nu	0.39	-0.09	-0.09
LF power	0.10	0.10	0.08
LF nu	-0.38	-0.44	-0.13
LF / HF	-0.37	-0.40	-0.38
Heart rate	-0.17	-0.13	-0.22
RMMSD	0.23	0.23	0.13
pNN50	0.21	0.20	0.03
SDNN	0.01	0.14	0.05
Total power	0.16	0.17	0.10
VLF HF	-0.23	-0.16	0.02
VLF Power	-0.10	-0.12	-0.12
Hurst Exponent	-	-0.11	-

together concatenated. The second setting is designed to mimic a situation, when a person is making just several short-term recordings during a single day and we want to predict the age based on them. The last setting is in the use of a single short-term recording for the same purposes.

In terms of data processing, at first, we checked the correlations of all the features described in section 2 with the chronological age of the individual, to select potential candidates for biomarkers. They are all shown in table 1 and the top-correlated features (both negatively and positively) are LFnu and LF/HF both from 24-hours and short term, recordings mean (positively correlated) and RMSSD, HFnu (negatively).

Before applying an algorithm that learns from data, input samples have to be prepared properly, i.e. normalized or scaled to satisfy certain range or distribution. In this work we have compared min-max scaling, max-abs scaling, normalization and z-score scaling and have chosen max-abs scaling as the one, that performs the most in terms of further explained metrics. This estimator scales and translates each feature individually such that

the maximal absolute value of each feature in the training set will be 1.0. It does not shift/center the data, and thus does not destroy any sparsity. To the output log-transformation was applied and after restored with exponentiation operation.

To validate the performance of the age prediction algorithm, we need to split a dataset into training and testing sets and use the first one for fitting the model and the second one for performance tracking.

We have used a well-known cross-validation scheme with 10 folds and after average the results to see the mean performance and its statistical significance. As the main performance metrics, R2 and mean absolute error (MAE) were chosen. R2 shows general correlation of the prediction with the real age and should be closer to 1.0 and MAE represents the error in the terms of the age prediction itself.

To visualize the dataset and obtain intuition about possible outliers, clusters and dependencies types, we have used principal component analysis (PCA) projection and t-SNE, see [9], projection on the 2D space. If any strong

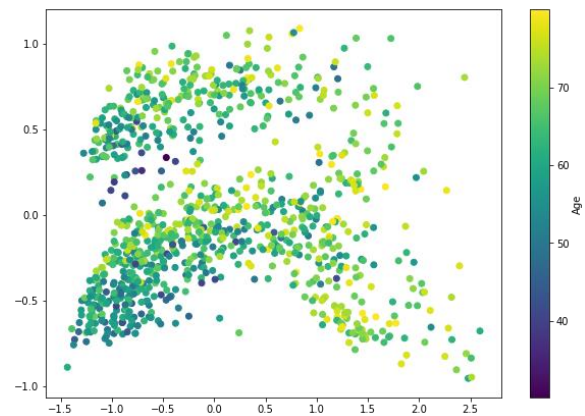


Fig. 3: PCA projection of all the features

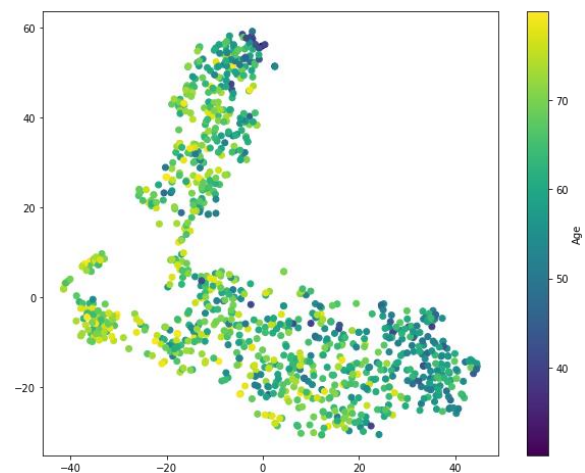


Fig. 4: t-SNE projection of all the features

linear dependencies are present, they will be shown on the PCA plot. Clusters and outliers are usually very well explained by the t-SNE embedding. As it can be seen from the figures X and Y, there is no strong linear dependence, but some clusters (of the mixed ages) are present, so we may hypothesis that strongly regularized linear model or non-linear estimators will be helpful in this case.

In this subsection, we will briefly describe regression models used in this work, motivation of the choices and main characteristics.

In machine learning, k-Nearest Neighbors Regression (kNN), see [10] for more details, is a non-parametric model that can be used both for classification and regression. The age is predicted by local interpolation of the targets associated with the k nearest neighbors in the training set. We can consider our dataset as the set of pairs $\{(X_i, Y_i)\}_{i=1 \dots N}$, where X_i is the i th individual ECG features and Y_i is its age. Given a distance in the space of $\{X_i\}$ and a member of this space X_j we can predict the age for it as such Y_j from $\{(X_i, Y_i)\}_{i=1 \dots N}$, where the distance between X_i and Y_j is the smallest. You can find more details on kNN regression in X.

This algorithm has several drawbacks, for example the need for storing all the dataset, but it is easy to implement and it is non-linear, which is our main assumption based on the visualizations of the data in the figures 3 and 4.

Linear assumption still can hold, as is shown in several works mentioned before. Then, the PCA and t-SNE plots can be explained with the redundant features in the dataset, that should be pruned, or taken into account with a smaller weight. It can be done with regularization, and one of the ways to do it is a ridge regression (see [11]). We rely on the Bayesian version of the algorithm (see [12] for more details) where we should learn a predictive distribution from the data to predict from it.

Ridge regression minimizes squared error while regularizing the norm of the parameters:

$$J(w) = \lambda w^2 + \sum_i (w^T X_i - Y_i)^2, \quad (1)$$

where J is a loss function, in our case mean squared error (MSE), w is the set of parameters of a linear model, X_i is the i th individual ECG features and Y_i is its age, λ is a regularization parameter

that, in our case, is inferred from the dataset itself.

Since the main hypothesis about the dependence between features and the age is that it is nonlinear, we need an appropriate model for it. There are several families of models designed to model nonlinear data, namely, polynomial models, neural networks, SVMs with different kernels and gradient boosting machines. We have chosen the latter, because they tend less to overfitting and work well with datasets that consist of numerous features of different types (categorical and numerical).

The idea behind gradient boosting regression, see [14] for more details, is in training an ensemble of so-called "weak learners", that is trained stage-wise. On each stage m , $1 < m < M$, the new member of an ensemble F_m is firstly considered as a weak model, that predicts the mean Y_i from the dataset. It is improved by constructing a new model $h(x)$ as $F_{m+1} = F_m + h(x)$, where $h(x)$ is found with gradient descent while optimizing a loss function J , see more details in [14].

Results. This section explains the performance of the trained algorithms within different experimental settings. On the table 3 the results of age prediction based on the features calculated from 24 hours, mean values of 6 short-term 5 minutes recordings and corresponding standard deviations. We see that gradient boosting regression performs reasonably well with MAE error close to 5 and high R^2 .

Table 4 shows how modeling of age based just on the mean values of 6 short-term 5 minutes recordings and corresponding standard deviations. As expected, the average performance dropped slightly, but not significantly. It proves our initial hypothesis, that age estimation can be done with several short-term measurements during the day.

Finally, we provide the results of regressing age based only on the feature set from a single short-term recording. The R^2 is very low and shows that predictions are not far from predicting the mean age value from the training set.

We also researched what particular features are the most important for the regression algorithm to understand top-performing biomarkers of aging. We extracted them from the gradient boosting regression model as the one

Table 2

24-hours features regression results

	Nearest Neighbors	Bayesian Ridge	Gradient Boosting
MAE	5.86 ± 0.64	5.47 ± 0.48	5.16 ± 0.41
R^2	0.31 ± 0.07	0.39 ± 0.04	0.41 ± 0.03

Table 3

Several short-term features regression results

	Nearest Neighbors	Bayesian Ridge	Gradient Boosting
MAE	7.3 ± 0.54	7.21 ± 0.78	6.97 ± 0.68
R^2	0.28 ± 0.03	0.33 ± 0.05	0.35 ± 0.02

that performed the best. We have used the model from the first experiment, which takes into account all the features both from the 24-hour and short-term recordings. The results are presented on fig. 5. As we can see, top-5 performing features are mean of LF/HF of short-term recordings, standard deviation of MxDMn of the short-term recordings, standard deviation of HystAmo of the short-term recordings, mean of HF of the short-term recordings and artefact standard deviation of the short-term recordings. It proves the hypothesis of usefulness of applicability of short-term recordings for the biological age estimation with ECG.

Additionally, we have performed an experiment with changing the objective function from regression to classification into age groups, each in the range of 10 years, to check how the features from our dataset are able to predict drastic changes in the age group. Eventually, it can be stated as 6-class classification, where with a 10-

Table 4

Single short-term features regression results

	Nearest Neighbors	Bayesian Ridge	Gradient Boosting
MAE	11.03 ± 1.2	10.9 ± 0.98	10.3 ± 0.9
R^2	0.05 ± 0.11	0.07 ± 0.2	0.8 ± 0.12

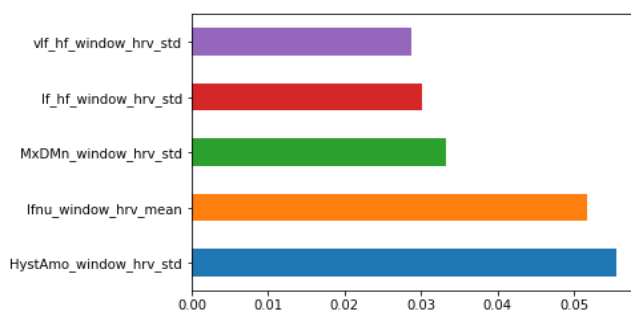


Fig. 5: Feature importance from gradient boosting regression

fold cross-validation scheme we could obtain 55 ± 0.71% accuracy.

Conclusions. In this work, we have explored the ECG as the source of biomarkers of aging. With the rise of popularity of wearable devices that are able to measure first-lead ECG, it could become an affordable and comfortable way to track the biological age of the heart and biological age of the person itself. We have collected and preprocessed a dataset of more than 1000 healthy individuals, compiling 3 experiments that aim to simulate a situation, when we predict the age based on the 24-hour continuous recording, several short, 5 minutes long, recordings per day and a single short recording accordingly. We have compared 3 different algorithmic approaches, namely, nearest neighbors similarity-based approach, Bayesian regression, and gradient boosting based regression. It is already a known result that we can predict hearts' biological age from the full 24-hours ECG recording, but we also show that with doing a couple of short-term recordings during a day, we can estimate this value with an acceptable loss of accuracy.

This research shows a room of consequent work both from the practical and theoretical point of view. First, it can be used for drug discovery research and to see how newly developed drugs affect the aging of the heart. Second, further experiments are needed with combining different sources of data from the wearable devices, like accelerometer-based data. Last but not least, from the theoretical point of view better algorithms for regression should be developed, that take into account more sophisticated age distributions and novel features have to be developed as well.

References.

1. Horvath S., DNA methylation age of human tissues and cell types. *Genome Biol.* 2013;14(10):R115.
2. Cells and Surveys: Should Biological Measures Be Included in Social Science Research? National Research Council (US) Committee on Population; Finch CE, Vaupel JW, Kinsella K, editors. Washington (DC): National Academies Press (US); 2001.
3. Toshiko Tanaka et al., Plasma proteomic signature of age in healthy humans *Aging Cell.* 2018 Oct; 17(5): e12799. Published online 2018 Jul 11. doi: 10.1111/accel.12799
4. Vito Starc, Manja Leban et al., Can Functional Cardiac Age be Predicted from the ECG in a Normal Healthy Population?
5. David Blokh, Ilia Stambler, The use of information theory for the evaluation of biomarkers of aging and physiological age *Mechanisms of Ageing and Development* Volume 163, April 2017, Pages 23-29
6. Natalia Botsva et al., Predictors of aging based on the analysis of heart rate variability *PACE*, Volume 40, Issue11, November 2017, Pages 1269-1278
7. Simon W Rabkin, Xin-Bo Justin Cheng, Detailed analysis of the impact of age on the QT interval *J Geriatr Cardiol.* 2016 Sep; 13(9): 740748.
8. Marcelo Franken, Amit Nussbacher, ST Elevation Myocardial Infarction in the elderly *J Geriatr Cardiol.* 2012 Jun; 9(2): 108114.
9. L.J.P. van der Maaten. Accelerating t-SNE using Tree-Based Algorithms. *Journal of Machine Learning Research* 15(Oct):3221-3245, 2014.
10. Altman, N. S. (1992). "An introduction to kernel and nearest-neighbor nonparametric regression". *The American Statistician.* 46 (3): 175185.
11. Section 3.3 in Christopher M. Bishop: *Pattern Recognition and Machine Learning*, 2006
12. David J.C. MacKay, *Bayesian Interpolation* Submitted to *Neural Computation* as a review paper, May 18, 1991
13. Roman . Baevsky, Anna G. Chernikova, Heart rate variability analysis: physiological foundations and main methods DOI: 10.12710/cardiometry.2017.10.6676
14. Friedman, J.H. (February 1999). "Greedy Function Approximation: A Gradient Boosting Machine"
15. <https://medlineplus.gov/ency/article/003877.htm>
16. <https://mawi.band>
17. <https://www.apple.com/apple-watch-series-4/health/>
18. <https://www.irhythmtech.com/>
19. <https://www.getqardio.com/>

**Yuzko R.V.,
Slobodian O.M.**

Department of Anatomy, Clinical Anatomy and Operative Surgery of the Bukovinian State Medical University, Chernivtsi, Ukraine

PECULIARITIES OF PERINATAL TOPOGRAPHY OF THE HEPATODUODENAL LIGAMENT COMPONENTS

Abstract. *A number of publications in the scientific periodical dealing with anatomical study of the structural components of the hepatoduodenal ligament are indicative of great interest of the scientific community in this issue. To determine macroscopic, anatomical and topographic peculiarities of the human hepatoduodenal ligament at the early period of ontogenesis, a complex of up-to-date methods of morphological study are used: macroscopic – for visual investigation of the state of the hepatoduodenal ligament components, injection of the vessels to study peculiarities and angioarchitectonic variants of the arterial components of the hepatoduodenal ligament, statistical – to determine peculiarities of morphological transformations of the hepatoduodenal ligament components and adjacent structures in different terms of the prenatal and postnatal periods of ontogenesis. Formation of the topography and syntopy variants of the hepatoduodenal ligament components (common bile duct, portal hepatic vein, proper hepatic artery) in fetuses and neonates is stipulated by close interrelations both between them and with the adjacent structures and organs. Additional components of the hepatoduodenal ligament are the common hepatic duct, cystic duct, right and left hepatic ducts, common hepatic artery found in 87,5 % of cases. Additional components of the hepatoduodenal ligament are more inherent for 6-10-month fetuses and neonates. During the perinatal period of ontogenesis the permanent components of the hepatoduodenal ligament are located in the sagittal plane in the following succession: the portal hepatic vein in all the cases is in the dorsal position concerning extra-hepatic bile ducts and arteries. In 60 % of observations the extra-hepatic bile ducts have a ventral position, and in 40 % of cases they have an intermediate position between dorsally located portal hepatic vein and ventrally located arteries. There are two types of arterial branching in the hepatoduodenal ligament during the fetal and early neonatal periods of ontogenesis: major one typical for early fetuses (75 %) and loose one found in the majority of cases of late fetuses and neonates (70 %).*

Key words: *hepatoduodenal ligament, portal hepatic vein, extra-hepatic bile ducts, perinatal period, fetus, anatomy, human.*

Introduction. A thorough investigation of the topographic-anatomical peculiarities, embryonic topography and perinatal anatomy of the organs and structures is essential not only to understand etiology and pathogenesis of mechanisms promoting development of congenital pathology, but to devise adequate methods of their correction. Considerable success has been achieved in modern development of hepatic surgery – one of the problematic fields of medicine. Nevertheless, partial resection of the liver remains one of the most complicated surgical procedures associated with certain topographic-anatomical peculiarities of the

hepatoduodenal ligament components. Therefore, it should be noted that in spite of the methods of partial resection of the liver a surgeon is facing the issues of hemostasis associated with the development of both intra- and postoperative complications [1, 4].

To avoid complications during surgery on the bile ducts with severe mechanical or obstructive jaundice is now an important issue of the abdominal surgery. The main task while performing this surgery is to provide derivation of bile from the liver to the alimentary tract with severe obstruction of the intra-hepatic ducts occurring due to scar strictures of the bile ducts,

congenital atresia, tumors, Echinococcus and other diseases in the bifurcation area of the bile and lobular hepatic ducts.

Making biliary-enteric anastomosis is the only possible way to treat mechanical/obstructive jaundice in patients with this pathology. Surgery on formation of anastomosis between the intra-hepatic ducts and gastrointestinal tract is complicated and is not often performed.

Liver resection in patients with severe obstruction of the bile ducts is known to be risky and traumatic due to a complicated access to the intra-hepatic ducts. Therefore, development of surgical access to the intra-hepatic ducts without liver resection is an urgent issue based on a detailed learning of their topography as well as topography of the hepatoduodenal ligament components [2, 5].

Nowadays stones in the gallbladder are found approximately in 10 % of adult population, more often among women at the age of 40 and older, and the number of complications remains invariably high. Therefore, qualitative radical treatment of patients with calculous cholecystitis is an important task of modern surgery. Solution of this task is based on a comprehensive examination of the topography of the gallbladder and extra-hepatic bile ducts. Irrespective the fact that every year the number of contraindications for laparoscopic cholecystectomy becomes smaller both with chronic and acute cholecystitis, general contraindications to perform endoscopy are the following: severe cardio-pulmonary pathology, coagulability or blood clotting disorders, peritonitis, inflammatory and infectious diseases of the abdominal wall, late terms of gestation. Though, in spite of the fact that the number of contraindications to perform laparoscopic cholecystectomy decreases quickly, the amount of postoperative complications remains comparatively high. Intraoperative complications stipulate transition to open surgery. Conversion ranges from 0,7 to 36 % cases. The main causes of conversion are: marked inflammatory process, commissural process, indications for choledochotomy, perforation of the gallbladder, injuries of the bile ducts and vessels, biliary-enteric abscesses, cancer of the gallbladder.

In spite of a considerable increase of the

number of endovideosurgery, the number and severity of iatrogenic intraoperative complications increases as well. As far as experience of laparoscopic surgery is accumulated, surgeons state about high variability in the structure of the hepatoduodenal ligament components. Every case of atypical location of the anatomical structures of the hepatobiliary area often results in the development of severe complications. Therefore, anatomical examination of a number of specimens taken from this portion will enable to considerably decrease the risk of complications including iatrogenic ones as well [3, 6].

Objective: to determine peculiarities of chronological succession of temporal transformations in the formation of topography and syntopy variants in the hepatoduodenal ligament components of fetuses and neonates.

Materials and methods. The study was conducted on 70 fetuses (25 isolated complexes of the abdominal organs and 45 dead fetuses) and 10 dead neonates. Museum specimens taken from the M.H. Turkevych Department of Human Anatomy, Department of Anatomy, Clinical Anatomy and Operative Surgery of Bukovinian State Medical University were used for the study. Successful combination of medical and methodological approaches during the investigation provided favourable conditions to obtain reliable results. Without consideration of their formation and development it is difficult to understand individual features and topographic-anatomical interrelations as the experience gives evidence. Thus, to understand the formation of the hepatoduodenal ligament not a separate age group should be taken for the study, but the dynamics of formation should be followed beginning from the early period of ontogenesis till birth. To determine macroscopic, anatomical and topographic peculiarities of the human hepatoduodenal ligament at the early period of ontogenesis, a complex of up-to-date methods of morphological study are used: macroscopic – for visual investigation of the state of the hepatoduodenal ligament components, injection of the vessels to study peculiarities and angioarchitectonic variants of the arterial components of the hepatoduodenal ligament, statistical – to determine peculiarities of

morphological transformations of the hepatoduodenal ligament components and adjacent structures in different terms of the prenatal and postnatal periods of ontogenesis.

The material was divided into age groups according to the classification of the human ontogenesis periods approved by VII All-Union Conference on the Issues of Age Morphology, Physiology and Biochemistry (Moscow, 1965), periods of the intrauterine development suggested by G.A.Shmidt (1968) and considering the "Instruction on Determining Criteria of the Perinatal Period, Live and Stillbirth", approved by the Order of the Ministry of Health of Ukraine dated 29.03.2006, № 179.

Results. The branches of the common hepatic artery have the utmost ventral position in fetuses of 4-month intrauterine development (161,0-200,0 mm of PCL) in 5 cases out of 10 (50 %). In the rest 50 % of cases the similar position was typical for the extra-hepatic bile ducts. That is, in a half of cases the right gastric artery and the right branch of the proper hepatic artery cross the common bile, cystic, right and left hepatic ducts in the front – from the ventral side. On the contrary, in the rest half of cases the extra-hepatic bile ducts cross the branches of the proper hepatic artery and the right gastric artery in front, that is, having the most ventral position in the hepatoduodenal ligament complex.

Arterial vessels in 5-month fetuses of the intrauterine development (fetuses of 201,0-250,0 mm PCL) in the majority of cases (7 out of 10) (70 %) pass behind the extra-hepatic bile ducts. Only in three cases (30 %) the arteries have the ventral position respectively. Similar to that in 6-month fetuses the arterial vessels in the majority of cases (6 out of 10) (60 %) are found to pass in the dorsal position concerning the extra-hepatic bile ducts. Opposite topography is found in 7-month fetuses, when in six out of ten cases the arterial vessels are in the ventral position concerning the extra-hepatic bile ducts, that is, the right gastric artery, the right branch of the proper hepatic artery, cystic artery cross the common bile, cystic, common hepatic, right and left hepatic ducts in front. 8-month fetuses of the intrauterine development (351,0-400,0 mm of PCL) have similar topography of those 4-month fetuses, that is, in a half of cases the right gastric artery and

branches of the proper hepatic artery including the cystic artery cross the extra-hepatic bile ducts: the common bile, cystic, right and left hepatic ducts from the ventral side. On the contrary, in the rest 50 % of cases the extra-hepatic ducts cross the branches of the proper hepatic artery and the right gastric artery in front, that is, they have the ventral position in the content of the hepatoduodenal ligament. In 9-month fetuses (401,0-450,0 mm of PCL) the arterial vessels in 6 cases (60 %) cross the extra-hepatic bile ducts and are in the ventral position concerning them, that is, the right gastric artery, the right branch of the proper hepatic artery, cystic artery cross the common bile, cystic, common hepatic, right and left hepatic ducts in front. Similar topography is found in 10-month fetuses (451,0-500,0 mm of PCL). The arterial vessels of neonates in 6 out of 10 cases (60 %) pass dorsally to the extra-hepatic bile ducts, that is, behind them (Fig. 1, 2).

The width of the hepatoduodenal ligament within its tubular structures changes from 4,0 mm at the beginning of the fetal period to 10,0 mm in neonates. The intensity of increasing the width of the hepatoduodenal ligament during the perinatal period is irregular. The most intensive increase occurs during the periods from 4 to 5 and from 8 to 9 months of the intrauterine development. These periods can be considered as the terms of an intensive development.

The length of the supra-duodenal portion of the common bile duct increases from 1,5 mm at the beginning of the fetal period to 12,0 mm in neonates. Intensity of increasing the length of the supra-duodenal segment of the common bile duct is the highest in the period of 4-5 and 7-8 months. These periods are suggested to be the terms of its intensive development. Morphometric

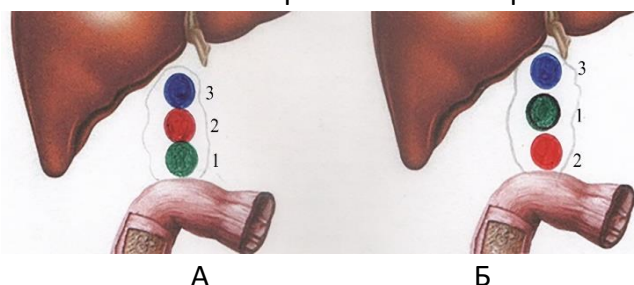


Fig.1. Schematic diagram of the topography of the hepatoduodenal intestinal components in the structure of the hepatoduodenal ligament. A – ventral location of the extra-hepatic bile ducts; B – ventral location of the arterial vessels. 1 – extra-hepatic bile ducts; 2 – arteries; 3 – hepatic portal vein.

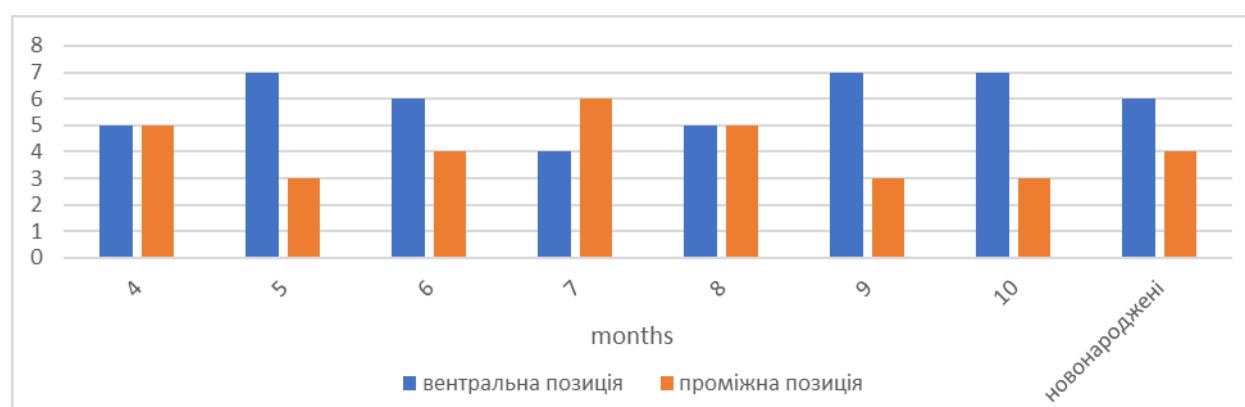


Fig 2. Topographic position of the extra-hepatic bile ducts in fetuses and neonates

parameters of the hepatoduodenal ligament during the perinatal period are presented in the Table.

The results of the skeletal-topographic examination performed by means of X-ray (Fig. 3) determined that the caudal extremity of the hepatoduodenal ligament is located on the level of the upper border of the twelfth thoracic vertebra. Its medial side is always projected on the level of continuation of the sternal line in the right to the anterior abdominal wall. The lateral wall of the ligament is projected differently depending on its width in the space between continuation of the median clavicular line and

anterior axial line to the anterior abdominal wall. The cranial extremity of the ligament is projected on the middle of the body of the eleventh vertebra and coincides with the location of the liver porta.

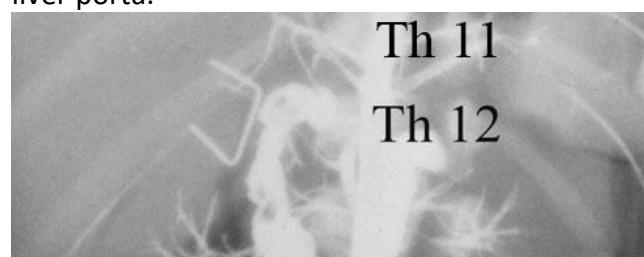


Fig. 3 Arteries and duodenum of the fetus (vessels and intestines are filled with injection mixture on the base of red lead). X-ray picture

Table

Morphometric parameters of the hepatoduodenal ligament during the perinatal period

Age (month)	Length of the hepatoduodenal ligament	Width of the hepatoduodenal ligament	Length of the gallbladder	Width of the gallbladder	Length of the upper portion of the duodenum	Width of the upper portion of the duodenum
4	5,22±0,50	3,29±0,22	5,88±0,27	2,05±0,18	5,25±0,05	3,24±0,06
5	8,55±0,68	6,49±0,28	8,72±0,70	2,30±0,13	6,33±0,23	4,23±0,09
6	7,62±0,48	6,18±0,21	11,25±0,45	3,03±0,16	6,35±0,18	4,87±0,13
7	10,25±0,48	7,95±0,47	13,60±0,88	3,80±0,22	6,96±0,15	5,28±0,08
8	15,17±1,04	10,28±0,51	18,50±0,67	4,40±0,14	6,98±0,16	5,33±0,08
9	20,80±1,20	11,92±0,37	20,80±0,25	5,09±0,09	8,91±0,15	5,68±0,10
10	27,91±1,09	16,99±0,79	21,39±0,57	5,32±0,13	9,66±0,12	6,56±0,16
Neonates	32,12±1,77	21,25±0,90	22,52±0,89	7,50±0,40	11,56±0,45	8,00±0,27

Discussion.

Examination of 80 specimens of dead fetuses and neonates determined certain peculiarities of the age perinatal anatomy of the hepatoduodenal

ligament structures. Peritoneal duplication is fixed by its one extremity to the liver porta, and by another one – to the upper wall of the duodenum. Its complex includes the following

tubular structures: portal hepatic vein, branches of the common hepatic artery, and extra-hepatic bile ducts.

Optogenetic transformations of the complex of the hepatoduodenal ligament structures are indicative of age changes of its shape. "Narrow" and "wide" shapes of the ligament are suggested to differentiate. A narrow shape is characterized by its trapezoidal form, and its components pass practically parallel. A wide shape of the ligament is characterized by the availability of a branched network of the tubular structures – the components of the hepatoduodenal ligament crossing between each other. Age transformations of the ligament's shapes are found in the study. At the beginning of the fetal period the fetuses of the 4-month intrauterine development (161,0-200,0 mm of PCL) in 80 % of cases have "narrow" ligament, that is, all its components are practically parallel to each other and cross at acute angles forming slit-like triangles including Calot's triangle. The number of "wide" ligament in 5-month fetuses is already twice as many – 40 %. 6-month fetuses possess "early" or "narrow" ligament less than "wide" ligament which is found in 60%. This rate is preserved till the end of the perinatal period. In 7 and 8-month of the intrauterine development only 10% of the hepatoduodenal ligament out of 20 specimens was found to have "narrow" type of branching of the tubular components. Only one case of "narrow" ligament was found in 9-month fetuses. The "narrow" ligament was not found in fetuses of the 10-month of the intrauterine development and neonates.

Conclusions. 1. Formation of the topography and syntopy variants of the hepatoduodenal ligament components (common bile duct, portal hepatic vein, proper hepatic artery) in fetuses and neonates is stipulated by close interrelations both between them and with the adjacent structures and organs.

2. Additional components of the hepatoduodenal ligament are the common hepatic duct, cystic duct, right and left hepatic ducts, common hepatic artery found in 87,5 % of cases. Additional components of the hepatoduodenal ligament are more inherent for 6-10-month fetuses and neonates.

3. The skeletal-topographic caudal extremity of the hepatoduodenal ligament is located on the level of the upper border of the twelfth thoracic vertebra. Its medial side is always projected on the level of continuation of the sternal line in the

right to the anterior abdominal wall. The lateral wall of the ligament is projected differently depending on its width in the space between continuation of the median clavicular line and anterior axial line to the anterior abdominal wall. The cranial extremity of the ligament is projected on the middle of the body of the eleventh vertebra and coincides with the location of the liver porta.

4. During the perinatal period of ontogenesis the permanent components of the hepatoduodenal ligament are located in the sagittal plane in the following succession: the portal hepatic vein in all the cases is in the dorsal position concerning extra-hepatic bile ducts and arteries. In 60 % of observations the extra-hepatic bile ducts have a ventral position, and in 40 % of cases they have an intermediate position between dorsally located portal hepatic vein and ventrally located arteries. There are two types of arterial branching in the hepatoduodenal ligament during the fetal and early neonatal periods of ontogenesis: major one typical for early fetuses (75 %) and loose one found in the majority of cases of late fetuses and neonates (70 %).

Список літератури:

1. Zatulokin VD, Perkov AA, Za EI. About a hemostasis at a resection of the left share of a liver *Journal of experimental and clinical surgery*. 2009;2(4):333-334.
2. Zatulokin VD, Grafov AK, Khalilov MA, Sheverdin NN, Alexeev AG. To the question of rational allocation of bilious channels of the left share of the liver. *Russian journal of pediatric surgery, anesthesia and intensive care*. 2015;5(2):13-9.
3. Batalova YuS, Kagan II, Nuzova OB. *Anatomo;surgical basis for optimization of laparoscopic cholecystectomy technique*. Perm Medical Journal. 2016;33(5):27-31.
4. Bednarsch J, Trauwein C, Neumann UP, Ulmer TF. Complication management after bile duct surgery. *Chirurg*. 2020 Jan;91(1):29-36. doi: 10.1007/s00104-019-01059-9.
5. Kadah A, Khoury T, Mahamid M, Assy N, Sbeit W. Predicting common bile duct stones by non-invasive parameters. *Hepatobiliary Pancreat Dis Int*. 2020 Jun;19(3):266-270. doi: 10.1016/j.hbpd.2019.11.003.
6. Röthlin M, Largiadèr F. The anatomy of the hepatoduodenal ligament in laparoscopic sonography. *Surg Endosc*. 1994 Mar;8(3):173-80. doi: 10.1007/BF00591825.

Malynovskyi A.

Ph. D. Student (System Analysis) of the Department of Mathematical Methods of System Analysis, NTUU "Igor Sikorsky KPI", Kyiv, Ukraine, E-mail: artem@mawi.band

MOBILE SYSTEM FOR ECG SIGNALS COLLECTION AND PROCESSING IN REAL-TIME

Abstract. *The article considers a system for collecting and processing electrocardiogram signals using wearable electrocardiographs. Measurement of electrocardiogram signals from such devices imposes additional requirements for signal processing, as the measurement takes place without the participation of doctors. Accordingly, control over the quality of measurement is entrusted to patients. A pipeline for real-time processing of electrocardiogram signals was built. The system architecture and each stage of signal processing are described. The FIR filter is used to filter the signal to remove low and high frequencies that contain signal noise. To test the system, the cardiograms of various people were collected from a wearable electrocardiograph. For validation of the electrocardiogram signals, a convolutional neural network (CNN) approach was selected. Resulting CNN was trained on the collected dataset. Additionally, an algorithm for validating the entire record based on the decision rules was created empirically. Testing of algorithms prediction accuracy and performance was performed. Results of this testing led to the conclusion that the system can work with high accuracy in real-time.*

Key words: ECG, CNN, validation, RPM

Introduction. Various wearable devices allow to measure human biosignals outside of the hospital and provide analysis of these biosignals or share measurements with doctors for expert analysis. This process is called Remote Patient Monitoring (RPM)[1]. This approach brings a lot of benefits to the healthcare system, but at the same time, it brings challenges for automated data analysis. Even with highly accurate devices, there is no guarantee that data will be measured correctly by the patient. Measurements are done outside the hospital, and as a result, without control of measurement correctness from the doctor's side.

Nowadays wearable devices for Lead I ECG measurement [2] have become widespread for Remote Patient Monitoring. Lead I ECG means the measurement of the signal between two electrodes located on the hands of the patient. These devices are designed to make short recordings of ECG signal for a heart health assessment, which can be done automatically or by manual doctor analysis. However, such an approach brings some challenges[3]:

- **Muscle noise** - appears if the patient is moving their hands or making too much pressure on the device during measurement.
- **Baseline wandering** - noise generated during the breathing process.

- **Signal inversion** - happens if a patient has swapped the hand location (put left hand on the electrode for the right hand and vice versa). In this case, the signal will be inverted which may lead to incorrect automatic analysis.
- **Other measurement issues.** Devices may be placed incorrectly (low contact with skin, too dry skin), so the recorded signal will be non-distinguishable from random noise.

Each measurement might be reviewed by a doctor, even after automatic analysis. In practice, doctors are interested in reviewing only measurements marked as "bad" - signals which were classified by automated analysis as signals with the potential presence of illnesses. The presence of problems described above may lead to misclassification, and as result to the unjustified expenses for the patients and the unwanted load of the doctors.

Various approaches for the ECG signal validation exist, but most of them were designed for validation of the signals from the holter devices (ECG recording under doctor's control, or using other leads)[4-5], or are not suitable for the use on the smartphones for the real-time ECG signal validation due to computational complexity, or low resulting accuracy[6-7]. Based on described challenges, a method for the real-

time ECG signal validation on the smartphone will be proposed in this paper.

This paper is organized as follows: first, full system architecture will be described in detail, with emphasis on how system components interact. Next, a data pipeline and various methods for ECG data processing inside this pipeline will be described. After this, a CNN-based architecture for ECG signal validation will be proposed. The final section contains the evaluation of the results and a discussion of the future work on the system.

System architecture

The proposed system architecture consists of 3 main parts(pic. 1):

- hardware device
- mobile application
- backend application

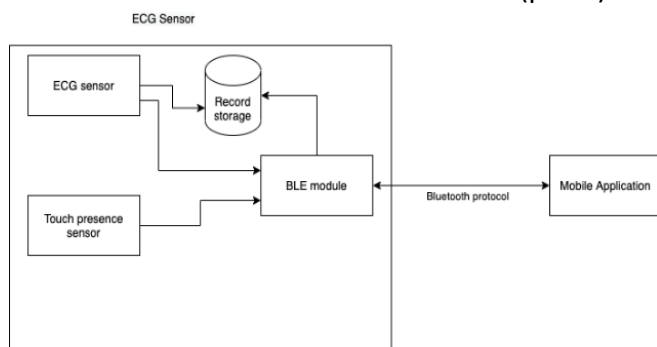


Pic. 1. System overview

This paper focuses on the mobile application part.

Hardware device

Lead I device for recording ECG with a sampling rate of 512 Hz. Device recording data to the buffer and streaming data over Bluetooth. Data bufferization is required to avoid packet loss, so the mobile application might be able to re-read missings packets. An algorithm for data integrity will be described in Section 3.2. Touch presence sensor tracks touch presence, to finish measurement if touch is absent. The high-level structure of the device is shown below(pic. 2):

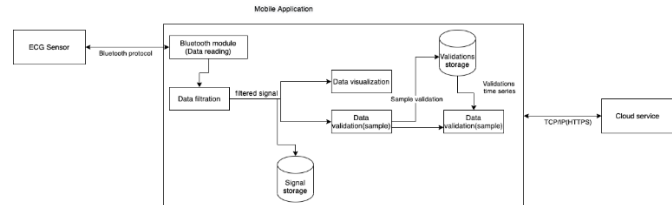


Pic. 2. High-level device architecture

Mobile application

A mobile application designed for the data reading, processing, and transmission to the cloud service for further data analysis and sharing with

the doctor for establishing a diagnosis. The mobile application structure is shown below(pic. 3):



Pic. 3. Mobile application structure

The purposes of each module shown above are following:

- **Bluetooth module:** Communication with the hardware device(data reading)
- **Data filtration:** Initial data pre-processing for further operations
- **Data visualization:** visualization of collected signal to the patient in real-time with validations results.
- **Data validation(sample):** Validation of each new sample with the convolutional neural network.
- **Data validation(full record):** Rule-based algorithm for validation of recorded signal for the final decision about the validity of the full record.

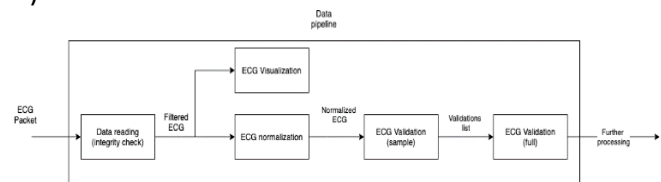
Cloud service

Cloud service is responsible for data storage, deep data analysis, and sharing measurements with doctors for making a diagnosis based on doctor's expertise and results of automated analysis.

Data processing pipeline

Pipeline overview

A pipeline that triggers each time as new points are packed is received from the sensor. From a data perspective process organized as follows(pic. 4):



Pic. 4. Data pipeline structure

Data reading

Communication with the device built on the "pub/sub" model. Mobile application subscribes to data recording from the device. Each received packet has an index number. If a new packet has index n+2 while the previous has index n - it means that packet with index n+1 was last. The

application will retry to receive a packet with a given index. If failed - the whole record will be marked as corrupted and measurement will be canceled. The record length used for this paper experiment was 90 seconds. Due to the algorithm of data integrity, data visualization and processing may lag behind the process of data reading(Algorithm 1).

Algorithm 1. Data reading integrity verification algorithm

Input. packet_index

Output. None

if packet_index -1 == last_received_index:

return

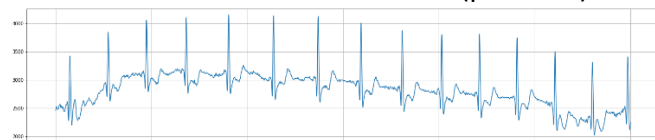
else:

request_packet_by_index(packet_index -

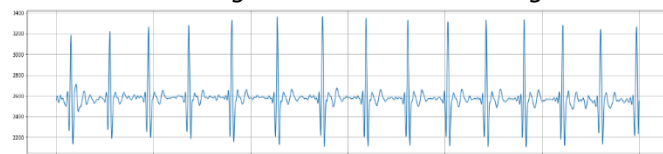
1)

Data filtering

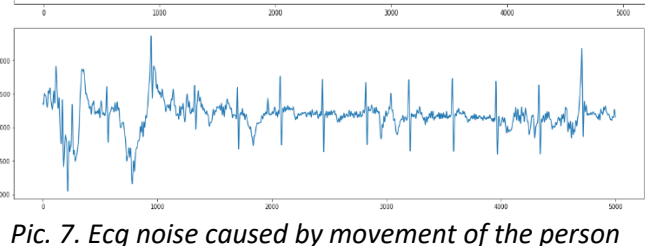
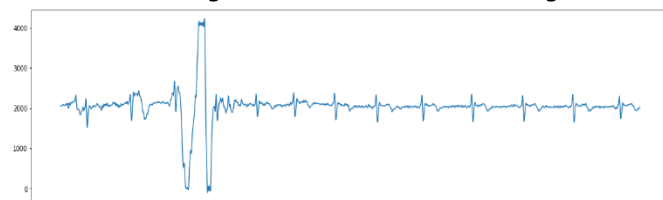
ECG is an electrical signal, and so it can be influenced by various types of noise. The most well-defined and easiest to counter type is power line interference. It happens when external alternating current influences ECG. Other types of noise include muscle noise which is caused by muscular electrical activity or noise caused by the movement of the person that conducts measurement. Influences of different types of noise on the ECG are shown below(pic. 5 - 7).



Pic. 5 - ecg with baseline wandering



Pic.6 - ecg without baseline wandering

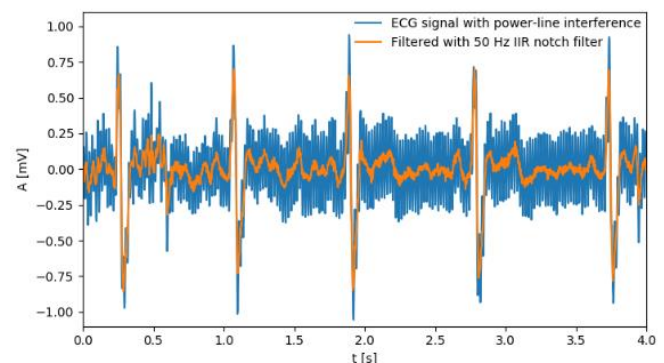


Pic. 7. Ecg noise caused by movement of the person

ECG analysis is not a new technique, and so a lot of ECG filtering approaches were developed. Most popular are FIR[8] and IIR[9] filtering. They are used to remove the noise of specific frequencies from the signal, and so the use of them is associated with some challenges. Often noise frequencies may overlap with frequencies of P waves and T waves of ECG. In this case filtering of these frequencies would affect the morphology of these waves, which is unacceptable for most cases of ECG analysis. Hence, there are two options:

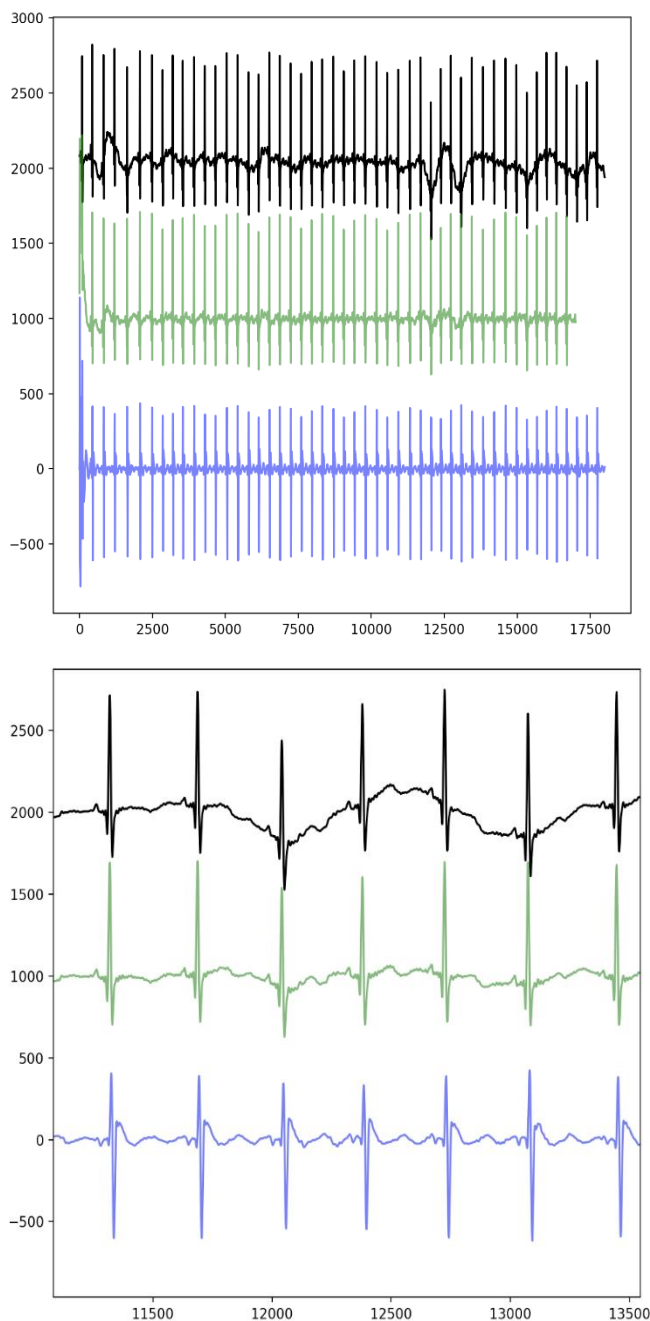
- Remove the frequency band that includes all the noise and alter the ECG morphology making the signal irrelevant for analysis in most cases. This approach may be applicable in some of the cases, such as Heart Rate Variability (HRV) analysis - when it's important to only accurately detect R waves.
- Use a frequency band that doesn't include P-wave and T-wave data and leave some noise in it.

Fortunately, the frequency of the alternating current is 50 Hz or 60 Hz depending on the country, and this frequency may be excluded from the signal without any risk(Pic. 8).



Pic. 8. Example of Power-line interference removal on ECG using IIR filtering

On the picture below(Pic. 9), you may see an example of filtering of ECG signal with FIR and IIR filters. Raw signal is displayed on the top, bandpass FIR filter with all the valuable frequencies inside the band in the middle and IIR filter that totally removes low-frequency noise (baseline wandering) but alters the morphology. Bandpass FIR filter with cutoff frequencies of 0.5 Hz and 40 Hz was selected for this implementation.



Pic. 9. Example of performance of FIR (green) and IIR (blue) filtering for noise removal on raw ECG signal (black)

Data preparation

For the data preparation was used normalization algorithm, to remove differences between records of different people related to the angle of the heart axis, which leads to the different projection of the signal:

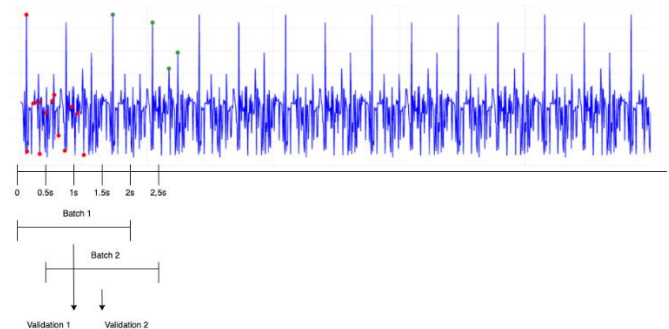
$$X_{normalized} = \frac{X - \text{mean}(X)}{\text{std}(X)},$$

where X - ECG points to an array of length 1000.

Data validation(sample)

Data validation performs using CNN for ECG signal validation(described in Section 4).

Validation performs on 1000 consecutive ECG points(2 seconds) with step 250 points(0.5 second). Validation results is a probability of Interference results are stored as time series used for full record data validation(Section 3.6). Validation process and validation array forming for the full record validation shown on the picture below(pic. 10)



Pic. 10. Data validation process

Data validation(full record)

Full record validation performs every time, new validations adds to the validations list, using the following algorithm(Algorithm 2):

Algorithm 2. Full record validation

Input. validations_list

Output. is_valid

```

if len(longest_sequence_invalid) >
  invalid_sequence_treshold:
  return False
if count(invalid_validations) >
  invalid_validations_treshold:
  return False
return True

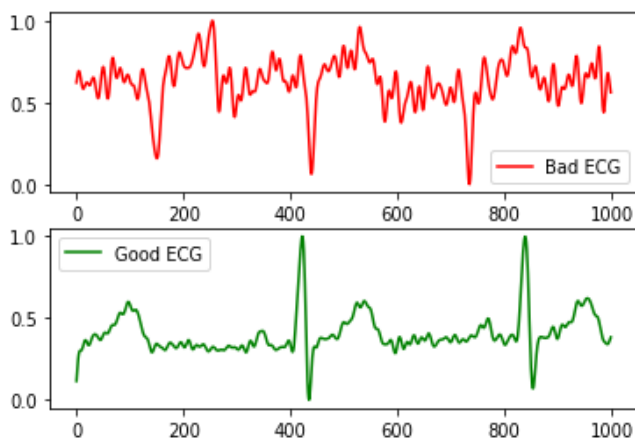
```

For record length 90 seconds (or 177 validations for window 1000 and step 250), were defined next parameters:

- longest_sequence_invalid = 17 (which represents 10 consecutive seconds of signal which wasn't recognized as ECG signal)
- invalid_validations_treshold = 88 (which represents value that equal to 50% of all validations performed for the record)

CNN for ECG signal validation

Deep convolutional neural networks (CNN) are known for their ability to learn complex visual patterns[11]. Therefore, the given technique was chosen for automatic ECG signal validation, since there is a visual difference between clear and corrupted signals as shown in the picture (pic .11).



Pic.11. Examples of bad (red) and good (green) ECG signals.

Approach description

Autoencoders (AE) are neural network architectures that in an unsupervised manner learn data representation by compressing and reconstructing it as close as possible to the input [12].

Given network is trained with a regular backpropagation algorithm, where loss function measures the difference between the actual object that was passed as the input and reconstruction at the output. In the case of ECG samples, the suitable loss is a mean squared error between input ECG and then reconstructed signal.

How to use the described approach for ECG validation, or for anomaly detection in particular? In this case, the task is to separate a set of “good” ECG signals from any other type of signal with significantly different morphology, which is called anomalies, or outliers. Such samples can occur because of muscle noise, movements, electrical inference, other noises, or even some inputs that did not contain any ECG signs. The most straightforward way to tackle this problem is to build a supervised learning model that solves binary classification for “noise”/“clear ECG”. However, in this case, the algorithm will not be robust for new unseen anomalies that weren't in the labeled dataset, so the model has to be retrained on an updated dataset that includes new anomalies. This approach is inconvenient for production use, thus a more stable approach will be described further.

To solve a given problem with AEs, the reconstruction error is used as the criteria of the anomaly. The given hypothesis is valid because if AE is trained only on ECG data and has not seen

any other type of signal, it will learn to reconstruct them quite accurately (with low mean squared error) [10]. In case of passing some noisy ECG or other non-ECG signals to the trained AE, it won't be able to reconstruct it (reconstruction error will be high compared to clear ECG samples).

In general, the algorithm of using AEs for anomaly detection contained the following steps:

1. Gather data of only correct ECGs
2. Train an AE to compress and reconstruct them
3. Calculate the average MSE (mean squared error) between ECGs and their reconstructions
4. Based on some samples of anomalies find a threshold alpha, where decision logic will be:
 - a. if error > alpha: this is an anomaly
 - b. else: it is good ECG

The above-described approach seems to work pretty well, but the major drawback is that there is no control on what exactly models take into account while deciding which ECG is good or bad. From the human expert perspective for current applications, such as ECG where the R peaks can be clearly seen (or probably not 100% clearly, but distinguishable by human experts). But the current model can't assure that it takes into account exactly present and visible R peaks, and detailed empirical analysis proves this point. We have seen samples, where reconstruction error was low, below the threshold, but there were no R peaks present and the opposite - an ECG sample with clearly seen R peaks could have had high reconstruction error.

The solution is in adding the second output to the model that predicts R peaks on the ECG sample making the model multiheaded. Now, the described model will not just reconstruct the ECG signal, but also predict R peaks on it. If both R peaks will not be found and reconstruction error is low, the ECG sample is accepted if the good one, if any of the conditions fails - a sample will be rejected as an anomaly. Thus, the algorithm changes to the following:

1. Gather data of only correct ECGs
2. Label R peaks on the ECGs
3. Train an AE to solve 2 tasks simultaneously:
 - a. compress and reconstruct ECG signal (MSE error)
 - b. find R peaks on the ECG (categorical cross-entropy error)

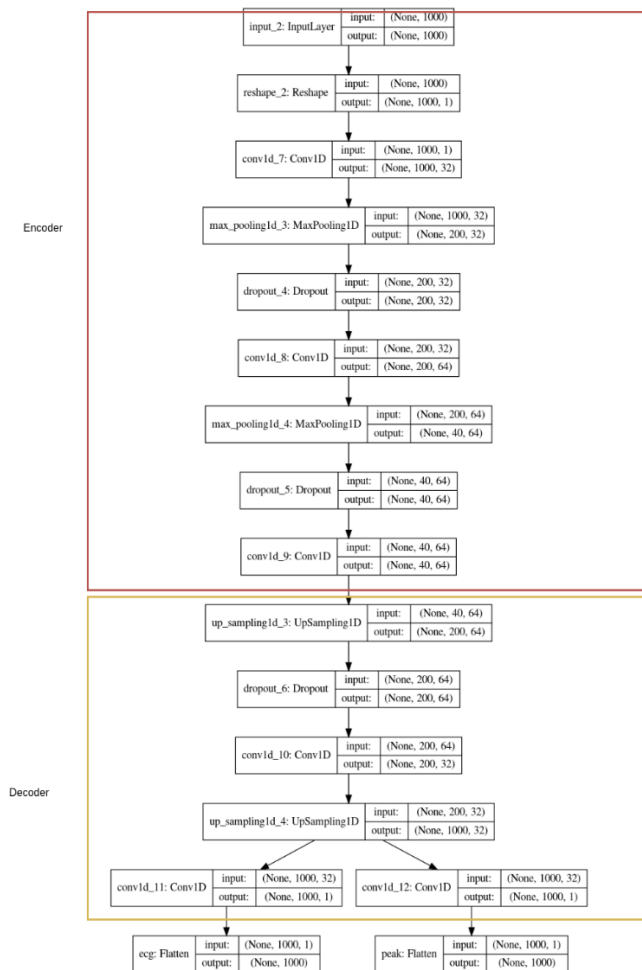
4. Calculate the average MSE (mean squared error) between ECGs and their reconstructions and save it as THRESH

5. Based on some samples of anomalies find a threshold alpha, where decision logic will be:

- if error \leq alpha AND at least one R peak found on ECG: it's good ECG
- else: it's an anomaly

Model architecture

The resulting architecture of CNN autoencoder with two heads for ECG signal validation, is shown below(pic. 12):



Pic. 12 Architecture of CNN for ECG signal validation

The network accepts 1000 points array as input, and has 2 outputs:

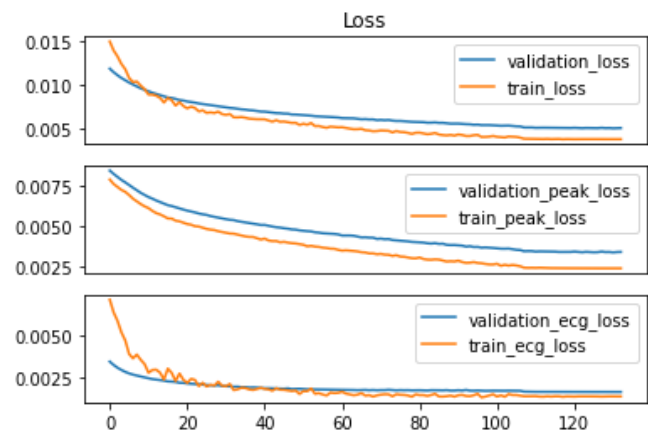
- ECG: reconstructed ECG sample
- peak: sparse vector with ones on points that correspond R-peaks on ECG signal

Dataset and model training

The training dataset contained 9392 pairs (raw signals, sparse vector with R-peaks). The validation set contained 3131 corresponding pairs. To adjust thresholds 6029 samples with

corrupted signal were used.

The network was trained with a regular backpropagation algorithm using Adam optimizer [13-14] with a learning rate of 0.001 during 150 epochs. Learning curves for total and separate losses (MSE and binary cross-entropy) change are shown on plots (pic). According to the plots, the learning stage performed well and validation all validation losses are low but slightly higher than training, reflecting the absence of overfitting(Pic. 13).



Pic.13. Losses during training

Results evaluation

Prediction performance

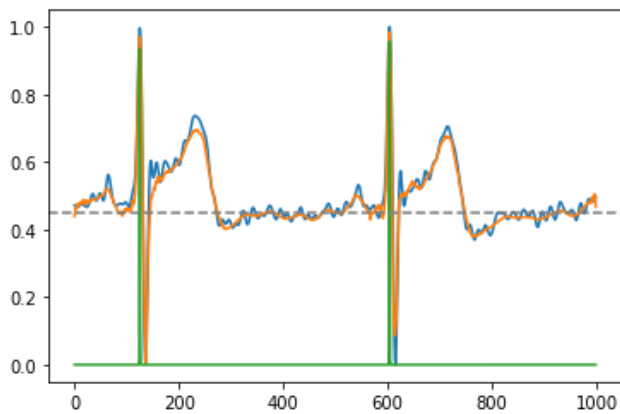
After training, a model was evaluated on a validation set and a set of corrupted samples. The resulting mean average error and maximal probability for each set can be seen in the table below(Table 1).

Table 1

Resulting mean average error and maximal probability

	Validation	Corrupted samples
MAE	0.0278201	0.02929014132
Mean max proba (MMP)	0.8442083	0.7556953

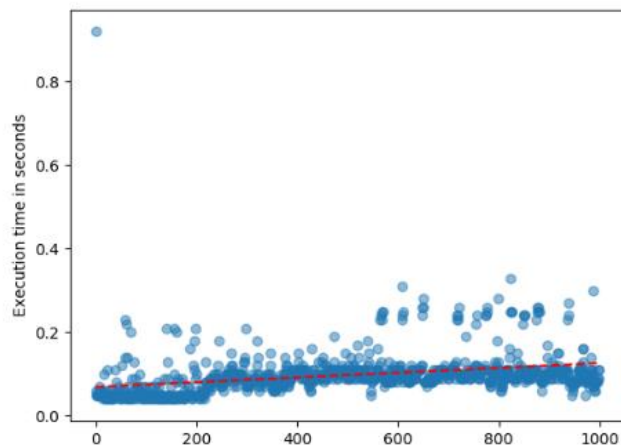
Based on obtaining results, decision thresholds were set to 0.075 for MAE and 0.45 for mean max probability. Given values provide quite an accurate separation between valid and noisy signals. An example of algorithm performance (MAE= 0.01609, MMP=0.9563) is shown on pic. with performance(Pic. 14).



Pic. 14. Model output (blue - original signal, yellow – reconstructed signal, green R-peak position prediction, dashed grey - MMP threshold)

Application performance

Results of data validation for samples of length 1000 points are shown below (Pic.15)



Pic. 15. Model inference speed performance

Received results display that's average model inference lasts for 0.2 seconds, which allows validating data in real-time with a window of 2 seconds (1000 points) and step of validation 0.5 seconds (250 points). Statically speaking validation ends earlier than the new batch for the validation becomes available. Which allows us to provide near real-time sample validation.

Conclusions

This article was dedicated to the processing of the ECG signals collected from wearable devices. Such devices have become very popular in healthcare for remote patient monitoring. However, since measurements with wearable devices are taken by patients without doctors' control, it may lead to incorrect measurements and as result to improper diagnosis with automated algorithms for disease detection, or by doctor manual review.

Typical problems related to measurements from wearable devices were described, and the architecture of the system for ECG signal collection and processing was developed. The architecture of the system includes algorithms for the data integrity check, algorithm for the noises removal, and data normalization for the ECG signal quality validation as the last stage.

For ECG signal quality validation were trained a convolutional neural network on the dataset collected from the wearable ECG monitor. This dataset was spilled on a dataset with a valid signal for training, and a corrupted signal for the test. All algorithms were deployed to the mobile application and works in near real-time mode, which allows giving fast feedback to the users about how properly they are measuring ECG signals.

In the future, might be suitable to design a more intelligent algorithm for the full record validation, since the current implementation was designed empirically. Also might be suitable to optimize algorithms for the lower analysis window size for faster feedback about measurement quality.

References:

1. Pekmezaris R, Mitzner I, Pecinka KR, Nouryan CN, Lesser ML, Siegel M, Swiderski JW, Moise G, Younker R Sr, Smolich K. The impact of remote patient monitoring (telehealth) upon Medicare beneficiaries with heart failure. *Telemed J E Health*. 2012 Mar;18(2):101-8. doi: 10.1089/tmj.2011.0095. Epub 2012 Jan 27. PMID: 22283360.
2. Al-Alusi MA, Ding E, McManus DD, Lubitz SA. Wearing Your Heart on Your Sleeve: the Future of Cardiac Rhythm Monitoring. *Curr Cardiol Rep*. 2019 Nov 25;21(12):158. doi: 10.1007/s11886-019-1223-8. PMID: 31768764; PMCID: PMC7777824.
3. Kumar P, Sharma VK. Detection and classification of ECG noises using decomposition on mixed codebook for quality analysis. *Health Technol Lett*. 2020 Feb 18;7(1):18-24. doi: 10.1049/htl.2019.0096. PMID: 32190336; PMCID: PMC7067057.
4. Naseri, Hosein. (2013). *Electrocardiogram Signal Quality Assessment Using Artificially Reconstructed Target Lead*. *Computer Methods in Biomechanics and Biomedical Engineering*.

5. Borisav Jovanović, Vančo Litovski, Milan Pavlović "QRS complex detection based ECG signal artefact discrimination". *Series: Electronics and Energetics* Vol. 28, No 4, December 2015, pp. 571 – 584
6. Vaclav Chudacek, Ľukas Zach, Jakub Kuzilek,, Jiri Spilka, Lenka Lhotska "Simple Scoring System for ECG Quality Assessment on Android Platform". *Department of Cybernetics, Faculty of Electrical Engineering, Czech Technical University in Prague, Czech Republic*
7. Zhao, Zhidong & Zhang, Yefei. (2018). SQI Quality Evaluation Mechanism of Single-Lead ECG Signal Based on Simple Heuristic Fusion and Fuzzy Comprehensive Evaluation. *Frontiers in Physiology*. 9. 10.3389/fphys.2018.00727.
8. J. A. Van Alste and T. S. Schilder, "Removal of Base-Line Wander and Power-Line Interference from the ECG by an Efficient FIR Filter with a Reduced Number of Taps," in *IEEE Transactions on Biomedical Engineering*, vol. BME-32, no. 12, pp. 1052-1060, Dec. 1985, doi: 10.1109/TBME.1985.325514.
9. Chavan, Mahesh & Agarwala, Ra & Uplane, Mahadev. (2008). *Suppression Of Baseline Wander And Power Line Interference in ECG Using Digital IIR Filter*. *International Journal of Circuits, Systems and Signal Processing*. 2.
10. LeCun, Y., Bengio, Y. & Hinton, G. Deep learning. *Nature* **521**, 436–444 (2015).
11. Z. Chen, C. K. Yeo, B. S. Lee and C. T. Lau, "Autoencoder-based network anomaly detection," 2018 *Wireless Telecommunications Symposium (WTS)*, Phoenix, AZ, 2018, pp. 1-5, doi: 10.1109/WTS.2018.8363930.
12. Peng Xiong, Hongrui Wang, Ming Liu, Suiping Zhou, Zengguang Hou, and Xiuling Liu. 2016. ECG signal enhancement based on improved denoising auto-encoder. *Eng. Appl. Artif. Intell.* 52, C (June 2016), 194–202. DOI:<https://doi.org/10.1016/j.engappai.2016.02.015>
13. Z. Zhang, "Improved Adam Optimizer for Deep Neural Networks," 2018 *IEEE/ACM 26th International Symposium on Quality of Service (IWQoS)*, Banff, AB, Canada, 2018, pp. 1-2, doi: 10.1109/IWQoS.2018.8624183.
14. Z. Zhang, "Improved Adam Optimizer for Deep Neural Networks," , Banff, AB, Canada, 2018, pp. 1-2, doi: 10.1109/IWQoS.2018.8624183.

Burianov O.A.

Dr.Med, Professor, Nationale Medizinische O. O. Bogomolez-Universität des Gesundheitsministeriums der Ukraine, 27 Bulvarno-Kudriavska St., Kyiv, Ukraine. ORCID: 0000 0001 8896 8371

Prozenko V.V.

Dr.Med, Professor, Staatliche Einrichtung „Institut für Traumatologie und Orthopädie der Nationalen Akademie der medizinischen Wissenschaften der Ukraine“, 27 Bulvarno-Kudriavska St., Kyiv, Ukraine. ip15@ukr.net. ORCID: 0000 0002 2174 1882

Obada Muhammad Bishtawi

Student, Staatliche Einrichtung „Institut für Traumatologie und Orthopädie der Nationalen Akademie der medizinischen Wissenschaften der Ukraine“, 27 Bulvarno-Kudriavska St., Kyiv, Ukraine ORCID: 0000 0001 7199 8208

Solonizyn J.O.

PhD, Facharzt für Orthopädie und Unfallchirurgie, Staatliche Einrichtung „Institut für Traumatologie und Orthopädie der Nationalen Akademie der medizinischen Wissenschaften der Ukraine“, 27 Bulvarno-Kudriavska St., Kyiv, Ukraine e-mail: eugenio.solonitsyn@gmail.com. ORCID: 0000 0001 7057 1405

Solovyov I.O.

Facharzt für Unfallchirurgie und Orthopädie, Krankenhaus Schongau GmbH, Marie-Eberth-Strasse 6, Schongau, Deutschland. Obere str. 14, 86971 Peiting, Deutschland. i.a.solovyov@gmail.com

ANALYSE VON ASEPTISCHEN PERIPROTHETISCHEN KOMPLIKATIONEN BEI KnieGELENKSTUMOREN JE NACH ART DER KnieGELENKSENDOPROTHESE

Zusammenfassung. Der Artikel berichtet über die Analyse von aseptischen periprotetischen Komplikationen bei Kniegelenkstumoren je nach Art der Kniegelenksendoprothese. Es wurden zwei Patientengruppen miteinander verglichen: die Hauptgruppe (n=31) bildeten die knieendoprothetischen Patienten, die die individuellen modularen Tumorendoprothesen der Firmen „Stryker“ (USA) und „Waldemar Link“ (Deutschland) erhielten, während die Kontrollgruppe (n=41) der knieendoprothetischen Patienten die individuellen Tumorendoprothesen der Firma „Inmed“ (Ukraine) implantiert bekam. Die vorgenommene Analyse ergab, dass sich die periprotetische Infektion, die aseptische Lockerung des Endoprothesenschaftes, der Knochenbruch an der Stelle, wo die Endoprothese mit ihrem Schaft eingepflanzt wird, und der Endoprothesenbruch als Hauptkomplikationen nach der Implantation von Tumorendoprothesen erwiesen. Es wurde festgestellt, dass pathologische Frakturen bei einem Tumor in der präoperativen Phase, verschiedene chirurgische Eingriffe in der präoperativen Phase, eine intraarterielle oder intravenöse Polychemotherapie sowie eine Strahlentherapie in der prä- und postoperativen Phase, die Tumorklassifikation, ein großer Knochendefekt nach der Resektion, eine übergroße Endoprothese, Defizit an Weichgewebe für die Abdeckung einer Endoprothese, Übergewicht, Begleiterkrankungen (Osteoporose, Diabetes mellitus u. a.), Tumorrückfälle und Nichteinhaltung des empfohlenen orthopädischen Regimes nachweislich das Risiko für eine aseptische Lockerung der Endoprothese und einen Knochenbruch im Bereich des Endoprothesenschaftes erhöhen.

Schlüsselwörter: Kniegelenk, Knochentumore, Endoprothetik, aseptische periprotetische Komplikationen.

Einleitung. Primäre Knochentumore haben einen relativ geringen Anteil an der Morbiditätsstruktur onkologischer Patienten und machen etwa 0,2-2,5 Prozent aller bösartigen Tumoren aus. [1,2]. Die das Kniegelenk bildenden Knochen sind in 60-70 Prozent der Fälle von malignen und benignen Tumoren betroffen. [3]. Bis in die 70-er Jahre des letzten Jahrhunderts standen bei einem tumorösen Befall der

Extremitätenknochen eine Amputation und eine Exartikulation der Extremität zur Wahl. [4]. Gegenwärtig kommt die Wahl zwischen einer organerhaltenden und einer zur Invalidisierung führenden Operation (Amputation, Exartikulation) nicht in Frage, denn es wird nach Möglichkeit eine organerhaltende Operation durchgeführt. Umstritten bleibt der Umfang des chirurgischen Eingriffs, der unter Einhaltung aller

Anforderungen in der orthopädischen Onkologie vorgenommen werden muss: 1) Radikalität unter möglichst niedrigem Risiko für den Patienten (Einhalten des Prinzips einer weiten Resektion und der Kompartimentresektion); 2) Ablastizität (Prävention des Tumorrezidivs); 3) Erhaltung der Extremität und ihrer Basisfunktionen [5]. Zurzeit gibt es einige grundlegende Rekonstruktionsmethoden nach Segmentresektion der kniegelenkbildenden Knochen – die Implantation von osteochondralen Allotransplantaten, Kombinationen aus Allotransplantat und Prothese, vaskularisierten Knochentransplantaten und maßgefertigten, patientenindividuellen Endoprothesen. Mit der Entwicklung neuer Chirurgiemethoden, Werkstoffinnovationen und Verbesserung des Endoprothesendesigns ist die Versorgung mit Endoprothesen ist wohl zum grundlegenden chirurgischen Behandlungsverfahren geworden und stellt den am häufigsten verwendeten Ansatz für die Behandlung von Tumoren im Kniegelenkbereich oder den Revisionseingriff bei sonstigen nicht-tumorösen Zuständen dar [6].

Mit der Zunahme chirurgischer Aktivitäten zugunsten organerhaltender Operationen steigt auch die Zahl der für die endoprothetische Versorgung charakteristischen Komplikationen an. In den ersten fünf Jahren nach der Arthroplastik nehmen die Infektionskomplikationen (19-38,5%) eine führende Stellung ein. Der zweithäufigste Revisionsgrund ist mit 16,1-36,5% die Instabilität der Endoprothesenkomponenten. Zu den selteneren Fällen, die zu einer Revision führen, gehören Beschädigungen am Implantat, periprothetische Frakturen und Fehlstellungen der Endoprothesenkomponenten [7, 8]. In der einschlägigen Literatur wird angegeben, dass bei Tumorlokalisation im distalen Femur nach Kniegelenksendoprothetik durchschnittlich bei 8% der Patienten Infektionskomplikationen, bei 10% aseptische Lockerung und bei 10% Rückfälle auftreten. Die allgemeine 5-Jahres-Haltbarkeit einer Endoprothese betrage etwa 54%. Ist der proximale Tibiaanteil betroffen, träten nach Kniegelenksendoprothetik bei 10-16% der Patienten Infektionskomplikationen, bei 18% aseptische Lockerung und bei 13% Rückfälle auf, wobei die allgemeine 5-Jahres-Haltbarkeit einer

Endoprothese etwa 38% betrage [9, 10, 11, 12]. Die Behebung dieser Komplikationen mit konservativen und chirurgischen Methoden, die eine systemische und lokale Antibiotikagabe, eine aktive Wunddrainage, das Entfernen von Implantaten und Knochenzement und eine einstufige Reendoprothetik mit einschließen, gelingt nur bei 27-30% der Patienten [13]. Die Versorgung des Kniegelenks mit einer Endoprothese führt insbesondere bei den Knochentumoren zur erheblichen Traumatisierung von Weichgewebe, einer ungleichmäßigen Belastungsverteilung am Knochen, einer Knochennekrose durch mechanische Bearbeitung, dem Einfluss der hohen Polymerisationstemperatur von Knochenzement auf den Knochen und einer Fremdkörperreaktion. Darüber hinaus ziehen die Reibstelle am künstlichen Gelenk und die Mikrobeweglichkeit einer Endoprothese und ihrer Komponenten eine aseptische Endoprothesenlockerung und die Knochenbrüche an der Stelle, wo die Endoprothese mit ihrem Schaft eingepflanzt wird, nach sich [14].

Bei den operierten Patienten mit Tumoren des Stütz- und Bewegungsapparates treten Faktoren auf, die zu Knochenschwäche führen können: 1) ein großer Umfang der Resektion von Weichgewebe, der die Extremitätenfunktion vermindert und somit zur Entwicklung einer Osteoporose beiträgt; 2) die Chemotherapie und die Strahlentherapie haben oft den Verlust an Knochenmasse zur Folge; 3) Schwäche des Muskelgewebes. Alles oben Genannte führt im Endeffekt zur Risikoerhöhung für Implantatinstabilität und eine Gang- und Standunsicherheit des Patienten [15].

In der letzten Zeit konnten die mit einer Infektion verbundenen Komplikationen dank der modernen antibakteriellen Präparate und der Weiterentwicklung von Chirurgietechnik verringert werden, auch die Häufigkeit von Tumorrezidiven ist durch die Anwendung von neuen Präparaten und einer zielgerichteten Therapie wesentlich zurückgegangen. Aktuelle Ingenieurinnovationen und der Einsatz von hochqualitativen Werkstoffen haben die Komplikationen seitens der Endoprothesenkonstruktionen erheblich reduziert. Ungelöst bleibt jedoch die Frage des

Knochengewebes (Fibrose, Verdünnung der Kortikalis mit anschließender Knochenresorption an der Grenze zum Implantat), wodurch seine biomechanischen Eigenschaften beachtlich gemindert werden [16].

In der Fachliteratur sind die Empfehlungen hinsichtlich der Behandlung einer periprothetischen Fraktur nach der Versorgung mittels Tumormegaprothesen immer noch nicht ausreichend und nicht konkret genug beleuchtet. Einer der Gründe wäre wohl die Diversifizierung der Modularprothesen in Bezug auf Länge, waren unterschiedliche Frakturtypen hervorruft. Zudem ist man sich gegenwärtig nicht einig über die Standardbehandlung von periprothetischen Frakturen bei solchen Patienten [17].

Demensprechend stellen die nach endoprothetischer Gelenkversorgung auftretenden Komplikationen ein bedeutendes Problem dar, das zu Funktionsstörungen, zuweilen auch zum Verlust einer Extremität führt und die Lebensqualität von Patienten, die aufgrund von Knochentumoren eine Kniegelenksendoprothese erhielten, erheblich beeinträchtigt.

Studienziel. Analyse von aseptischen periprothetischen Komplikationen nach endoprothetischer Versorgung des Kniegelenks bei Kniegelenkstumoren.

Material und Methoden. 72 Patienten mit lokal aggressiven und malignen Knochentumoren (wovon 31 Patienten die Hauptgruppe und 41 weitere die Kontrollgruppe bildeten), die in der Staatlichen Einrichtung „Institut für Traumatologie und Orthopädie der Nationalen Akademie der medizinischen Wissenschaften der Ukraine“ behandelt wurden, wurden mit Kniegelenksendoprothesen versorgt.

Zwecks Eruiierung der Wirksamkeit von entwickelten Methoden zur Kombinations- und Komplexbehandlung untersuchte man die wichtigsten prognostischen Parameter der gleichartigen Patientengruppen (Alter, Geschlecht, histologischer Aufbau der Neubildung, Tumorstadium). Die Verteilung der Patienten nach Alter und Geschlecht ist in der Tabelle 1 dargestellt.

Das Durchschnittsalter der Patienten betrug $26,9 \pm 1,25$ Jahre.

Nach der Tumorlokalisation im Bereich der kniegelenkbildenden Knochen verteilten sich die Patienten wie folgt (siehe Tabelle 2).

Die Verteilung der Patienten nach dem histologischen Tumortyp und Geschlecht ist in der Tabelle 3 dargestellt.

Die Verteilung der Patienten mit Knochentumoren nach dem histologischen Tumortyp und Tumorstadium ist in der Tabelle 4 dargestellt. Patienten, die mit Kniegelenksendoprothesen versorgt wurden, waren in zwei Gruppen eingeteilt: die Hauptgruppe (n=31) bildeten die knieendoprothetischen Patienten, die die individuellen modularen Tumorendoprothesen der Firmen „Stryker“ (USA) und „Waldemar Link“ (Deutschland) erhielten, während die Kontrollgruppe (n=41) der knieendoprothetischen Patienten die individuellen Tumorendoprothesen der Firma „Inmed“ (Ukraine) implantiert bekam.

Physikalisch-chemische Eigenschaften von Endoprothesen. Bei der Herstellung von Endoprothesen der Firma W. Link wird die Titan-Aluminium-Vanadium-Gusslegierung TiAl6V4 nach ASTM F1108 verwendet.

Tabelle 1

Verteilung der Patienten nach Alter und Geschlecht

Geschlecht \ Alter	10-19 (%)	20-29 (%)	30-39 (%)	40-50 (%)	über 50 (%)	INSGESAMT
Männer	10 (13,89%)	10 (13,89%)	10 (13,89%)	6 (8,33%)	4 (5,56%)	40 (55,56%)
Frauen	8 (11,11%)	7 (9,72%)	8 (11,11%)	4 (5,56%)	5 (6,94%)	32 (44,44%)
INSGESAMT	18 (25,0%)	17 (23,61%)	18 (25,0%)	10 (13,89%)	9 (12,5%)	72 (100%)

Tabelle 2

Tumorlokalisation im Bereich der kniegelenkbildenden Knochen

Lokalisation	Männer, (%)	Frauen, (%)
Distales Femur	26 (36,11 %)	19 (26,39 %)
Proximale Tibia	14 (19,44 %)	13 (18,06 %)
INSGESAMT	40 (55,55 %)	32 (44,45 %)

Tabelle 3

Verteilung der Patienten nach dem histologischen Tumortyp und Geschlecht

	Männer, (%)	Frauen, (%)
Osteogenes Sarkom	16 (22,22%) (zentral - 11, teleangiektatisch - 3, periosteal - 1, gemischt - 1)	10 (13,89%) (zentral - 6, parosteal - 2, teleangiektatisch - 1, gemischt - 1)
Riesenzelltumor des Knochens	12 (16,67%)	14 (19,44%)
Chondrosarkom	4 (5,56%)	3 (4,17%)
Malignes Riesenzelltumor des Knochens	3 (4,17%)	2 (2,78%)
Fibrosarkom des Knochens	2 (2,78%)	2 (2,78%)
Malignes fibröses Histiozytom des Knochens	2 (2,78%)	-
Ewing-Sarkom	1 (1,39%)	-
Metastatischer Tumor (Adenokarzinommetastase in der Schilddrüse)	-	1 (1,39%)
INSGESAMT	40 (55,56%)	32 (44,44%)

Tabelle 4

Verteilung der Patienten mit Knochentumoren nach dem histologischen Tumortyp und Tumorstadium

Histologischer Tumortyp	Patientenzahl	Tumorstadium						
		IA	IB	IIA	IIB	III	IVA	IVB
Osteogenes Sarkom	26	-	1	4	18	-	-	3
Riesenzelltumor des Knochens	26	-	-	-	-	-	-	-
Chondrosarkom	7	-	-	3	4	-	-	-
Malignes Riesenzelltumor des Knochens	5	-	-	2	3	-	-	-
Fibrosarkom des Knochens	4	-	-	2	2	-	-	-
Malignes fibröses Histiozytom des Knochens	2	-	-	-	2	-	-	-
Ewing-Sarkom	1	-	-	-	1	-	-	-
Metastatischer Tumor	-	-	-	-	-	-	-	1
INSGESAMT	72	-	1	11	30	-	-	4

Chemical composition / Chemische Zusammensetzung

Element	Name des Elementes (DE)	Name of element (EN)	Value (unit)/ Wert (Einheit)
Fe	Eisen	Iron	Max. 0,30%
C	Kohlenstoff	Carbon	Max. 0,10 %
H	Wasserstoff	Hydrogen	Max. 0,015 %
N	Stickstoff	Nitrogen	Max. 0,05 %
O	Sauerstoff	Oxygen	Max. 0,20 %
Al	Aluminium	Aluminium	5,5 – 6,75%
V	Vanadium	Vanadium	3,5 – 4,5 %
Ti	Titan	Titanium	Rest

Mechanical properties / Mechanische Eigenschaften

Symbol	Bezeichnung (DE)	Description (EN)	Value (unit)/ Wert (Einheit)
≤ Ø 40 mm			
R _m	Zugfestigkeit	Tensile strength	860 N/mm ² (MPa)
R _{p0,2}	Dehngrenze 0,2%	Yield strength	758 N/mm ² (MPa)
A	Dehnung	Elongation	Min. 8 %
Z	Brucheinschnürung	Reduction of area	Min. 14 %

Sterilisation. Die Implantate der Firma Waldemar Link GmbH & Co. werden mit einem geprüften Verfahren durch Gammastrahlen sterilisiert. Der SAL-Wert beträgt 10^{-6} . Der Gammasterilisationszyklus wurde nach ISO 11137-1 „Sterilisation von Produkten für die Gesundheitsfürsorge - Strahlen - Teil 1: Anforderungen an die Entwicklung, Validierung und Lenkung der Anwendung eines Sterilisationsverfahrens für Medizinprodukte“ entwickelt und validiert.

Das eingerichtete Überwachungssystem beinhaltet eine umfangreiche routinemäßige Kontrolle, einschließlich der Verifikationsdosis-Experimente, der Bioburden-Bestimmung, der Prüfungen auf Endotoxine sowie einer regelmäßigen Kontrolle aller Parameter. Die gammasterilisierten Produkte der Waldemar Link GmbH & Co. werden steril geliefert. Die Sterilitätsdauer beträgt fünf Jahre, es sei denn, dass die Verpackung beschädigt ist oder die Lagerung nicht sachgemäß erfolgt.

Die Verteilung der Patienten mit

Knochtumoren nach dem histologischen Tumortyp und Tumorlokalisation (Hauptgruppe) ist in der Tabelle 5 dargestellt.

Die Verteilung der Patienten mit Knochtumoren nach dem histologischen Tumortyp und Tumorlokalisation (Kontrollgruppe) ist in der Tabelle 6 dargestellt.

Die präoperative Untersuchung der Patienten umfasste eine klinische und röntgenologische Untersuchung (unter anderem eine CT- und MRT-Untersuchung, falls erforderlich) sowie eine obligatorische Stanzbiopsie oder offene Biopsie aus dem betroffenen Knochensegment zur Verifizierung des Prozesses. Nach der Untersuchung wurden für alle Patienten aufgrund der Röntgen-, CT- oder MRT-Befunde die Resektionsgrenzen fürs Knochensegment und die Größe der Endoprothese bestimmt.

17 Kranke (23,61%) wiesen pathologische Frakturen mit Tumorbefall auf, was die präoperative Untersuchung in hohem Maße erschwerte und zusätzliche technische Schwierigkeiten während der Operation und in

Tabelle 5

Verteilung der Patienten mit Knochtumoren nach dem histologischen Tumortyp und Tumorlokalisation (Hauptgruppe)

Histologischer Tumortyp	Lokalisation	
	Distales Femur	Proximale Tibia
Osteogenes Sarkom	11	5
Riesenzelltumor des Knochens	4	4
Chondrosarkom	2	1
Malignes Riesenzelltumor des Knochens	1	-
Malignes fibröses Histiozytom des Knochens	1	-
Ewing-Sarkom	1	-
Fibrosarkom des Knochens	-	1
INSGESAMT	20	11

Tabelle 6

Verteilung der Patienten mit Knochtumoren nach dem histologischen Tumortyp und Tumorlokalisation (Kontrollgruppe)

Histologischer Tumortyp	Lokalisation	
	Distales Femur	Proximale Tibia
Riesenzelltumor des Knochens	9	9
Osteogenes Sarkom	7	3
Chondrosarkom	3	1
Malignes Riesenzelltumor des Knochens	3	1
Fibrosarkom des Knochens	2	1
Malignes fibröses Histiozytom des Knochens	-	1
Metastatischer Tumor	1	-
INSGESAMT	25	16

der nachfolgenden Rehabilitation bereitete.

Bei 10 Patienten (13,89%) hatte man vor der eigentlichen endoprothetischen Kniegelenksoperation verschiedenartige chirurgische Eingriffe (osteoplastische Operationen unter Verwendung von Auto- und Alлотransplantaten, Hydroxylapatit- und Tricalciumphosphat-Keramiken und bioaktiven Glaswerkstoffen sowie verschiedene Arten der Metallosteosynthese) an ihrem Wohnort vorgenommen, was bei der Entwicklung von postoperativen Komplikationen auch mitwirkte.

Bei 37 (51,39%) Kranken wurde eine intraarterielle oder intravenöse Polychemotherapie in der prä- und postoperativen Phase durchgeführt.

7 (9,72%) Patienten erhielten in der präoperativen Phase eine Strahlentherapie bis zum Erreichen einer Herddosis (HD) von 40 Gy, was bei der Entwicklung von postoperativen Komplikationen ebenfalls eine Rolle spielte.

Der chirurgische Eingriff wurde im folgenden Umfang vorgenommen: Nach der En-bloc-Resektion des Knochentumors wurde der Knochendefekt entweder durch eine individuelle Tumorendoprothese der Marke „Inmed“ oder durch eine individuelle modulare Tumorendoprothese der Marken „Stryker“ bzw. „W. Link“ ersetzt. Am 2. postoperativen Tag wurden die Patienten unter Zuhilfenahme von Unterarmgehstützen oder eines Rollators bei eingeschränkter Belastung der operierten Extremität vertikalisiert und mobilisiert. Nach dem Entfernen von Nahtmaterial (am 14. postoperativen Tag) wurde den Patienten eine dosierte und zunehmende Belastung der operierten Extremität, Krankengymnastik und Mechanotherapie bis zum Ablauf von zwei Monaten empfohlen. Nach 2 Monaten wurden die Patienten postoperativ nachuntersucht, um funktionelle und onkologische Ergebnisse klinisch und röntgenologisch zu erheben.

Die funktionellen Ergebnisse nach einer Operation an der Extremität wurden anhand des MSTS-Score ermittelt. Die Lebensqualität wurde mit dem QLQ-C30 Fragebogen der EORTC beurteilt. Die Überlebensrate von Patienten wurde nach der Kaplan-Meier-Methode geschätzt.

Ergebnisse und ihre Beurteilung. In der

Hauptgruppe der Patienten (n=31), die mit modularen Endoprothesen der Firmen „Stryker“ und „Waldemar Link“ versorgt wurde, waren bei 8 Patienten (25,8%) nach Endoprothetik des Kniegelenks bei Tumorlokalisation im distalen Femur Komplikationen zu beobachten – die aseptische Lockerung des Prothesenschaftes bei 6 (19,35%), periprothetische Infektion bei 1 (3,23%) und Endoprothesenbruch ebenfalls bei 1 Patienten (3,23%). Tumorrezidive wurden bei 2 Patienten (6,45%) dieser Gruppe festgestellt. 6 (19,35%) hatten Lungenmetastasen. 2 Patienten (6,45%) sind während der Therapie an Lungenmetastasen gestorben. Nach der Endoprothesenversorgung bei Tumorlokalisation in der proximalen Tibia wurden bei 2 (6,45%) Patienten Komplikationen beobachtet - 1 (3,23%) erlitt eine aseptische Lockerung des Prothesenschaftes und 1 (3,23%) erlitt eine periprothetische Infektion. In dieser Gruppe wurden keine Tumorrezidive festgestellt. 2 (6,45%) Patienten besaßen Lungenmetastasen. 1 (3,23%) Patient ist während der Therapie an Lungenmetastasen gestorben.

In der Kontrollgruppe der Patienten (n=41), die mit Kniegelenksendoprothesen der Firma „Inmed“ versorgt wurde, waren bei 14 (34,15%) der Patienten nach Endoprothetik bei Tumorlokalisation im distalen Femur Komplikationen zu beobachten - periprothetische Infektion bei 7 (17,07%), die aseptische Lockerung des Prothesenschaftes bei 4 (9,76%), Femurfraktur bei 2 (4,88%) und Endoprothesenbruch bei 1 Patienten (2,44%). Bei 2 Patienten (4,88%) dieser Gruppe wurden Tumorrezidive festgestellt. 2 (4,88%) hatten Lungenmetastasen. 3 Patienten (7,32%) sind während der Therapie an Lungenmetastasen gestorben. Bei Tumorlokalisation in der proximalen Tibia wurden nach Endoprothetik bei 9 (21,95%) Patienten Komplikationen beobachtet – periprothetische Infektion bei 4 (9,76%), Schienbeinbruch bei 3 (7,32%), die aseptische Lockerung des Prothesenschaftes bei 1 (2,44%) und Endoprothesenbruch ebenfalls bei 1 Patienten (2,44%). Bei 1 Patienten (2,44%) dieser Gruppe wurde ein Tumorrückfall festgestellt. 1 (2,44%) hatte Lungenmetastasen. 1 Patient (2,44%) ist während der Therapie an Lungenmetastasen gestorben.

Bei den Patienten der Gruppe mit Kniegelenksendoprothesen der Firma „Inmed“ wurde nach distaler Femurresektion und Kniegelenksendoprothetik das funktionelle Ergebnis mit einem MSTS-Score von durchschnittlich 82,4 % erzielt, während der durchschnittliche funktionelle MSTS-Score nach proximaler Tibiaresektion 76,2 % betrug. Nach der Verwendung von modularen Endoprothesen von "Stryker" und "Waldemar Link" betrug der durchschnittliche funktionelle MSTS-Score 90,1 % nach distaler Femurresektion und Kniegelenksendoprothetik bzw. 82,2 % nach proximaler Tibiaresektion und Kniegelenksendoprothetik.

Die durchschnittliche 3- und 5- Jahres-Überlebensrate von Implantaten betrug für die Endoprothesen der Firmen "Stryker" und "Waldemar Link": nach 1 Jahr - 1,0, nach 2 Jahren - 1,0, nach 3 Jahren - 1,0, nach 4 Jahren - 0,95 und nach 5 Jahren - 0,9; für die Endoprothesen der Firma „Inmed“: nach 1 Jahr - 0,95, nach 2 Jahren - 0,85, nach 3 Jahren - 0,73, nach 4 Jahren - 0,65 und nach 5 Jahren - 0,5.

Die Lebensqualität von Patienten ist nach endoprothetischer Versorgung des Kniegelenkes mit Endoprothesen der Firmen "Stryker" und "Waldemar Link" (EORTC-QLQ-C30-Fragebogen) von 45 auf 84 Punkte, nach der Versorgung mit Endoprothesen der Firma „Inmed“ von 45 auf 72 Punkte angestiegen.

Die allgemeine 3-Jahres-Überlebensrate von Patienten betrug $82,2 \pm 1,4\%$ ($p > 0,05$), die 5-Jahres-Überlebensrate betrug $65,8 \pm 2,6\%$ ($p > 0,05$).

Es seien Fallbeispiele aus der Praxis angeführt. Ein Beispiel für eine aseptische Lockerung des Prothesenschaftes: Die Patientin G., 42 Jahre alt, Patientenakte Nr. 000000, wurde im Juli 2015 aufgrund eines Riesenzelltumors des distalen Femurs in einer Abteilung der Staatlichen Einrichtung „Institut für Traumatologie und Orthopädie der Nationalen Akademie der medizinischen Wissenschaften der Ukraine“ operiert (Tumorresektion mit distaler Femurresektion und endoprothetische Versorgung des Kniegelenks mit einer individuellen modularen Tumorendoprothese der Firma „Stryker“). Die Patientin hatte in der präoperativen Phase eine Strahlentherapie mit einer Gesamtdosis von 40 Gy am

onkologischen Dispensaire an ihrem Wohnort erhalten. 2018 trat eine aseptische Lockerung des Endoprotehsenschaftes im Oberschenkelknochen, die sie auf schwere körperliche Arbeit zurückführte. Im Juli 2018 wurde nach einer Nachuntersuchung der Patientin eine Wechselendoprothetik am Kniegelenk durchgeführt, die postoperative Periode verlief ohne Komplikationen. Die Verlaufskontrolle zeigt nach dem Stand vom August 2020, dass die Patientin ein gutes Allgemeinbefinden hat, klinisch und röntgenologisch ist keine aseptische Lockerung des Endoprothesenschaftes im Oberschenkelknochen festgestellt worden. In Abbildung 1 sind Röntgenaufnahmen dargestellt, die bei der Patientin G. nach der aseptischen Lockerung des Endoprotehsenschaftes der Firma „Stryker“ im Oberschenkelknochen und der Wechselendoprothetik am Kniegelenk angefertigt wurden.

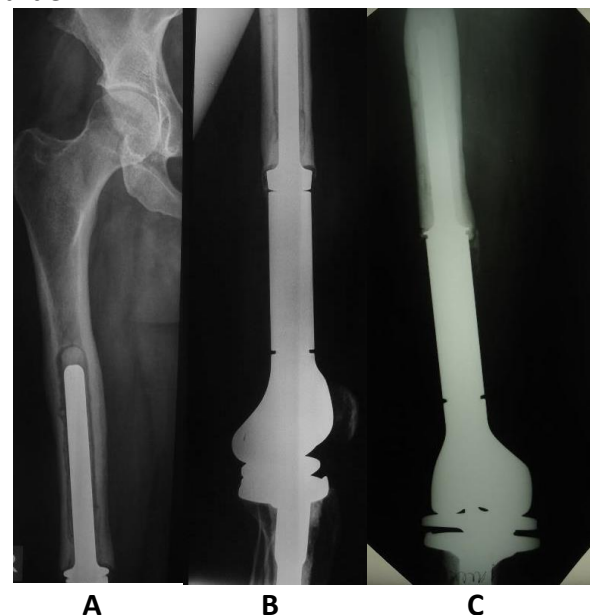


Abbildung 1. Röntgenaufnahmen des rechten Oberschenkels der Patientin G.: a) und b) Zustand nach endoprothetischer Versorgung des Kniegelenks mit einer Endoprothese der Firma „Stryker“ bzw. aseptische Lockerung des Endoprotehsenschaftes im Oberschenkelknochen; c) Zustand nach Wechselendoprothetik.

Der Patient M., 33 Jahre alt, Patientenakte Nr. 565265, wurde im Mai 2010 aufgrund eines Osteosarkoms des distalen Femurs in einer Abteilung der Staatlichen Einrichtung „Institut für Traumatologie und Orthopädie der Nationalen Akademie der medizinischen Wissenschaften der Ukraine“ operiert (Tumorresektion mit distaler

Femurresektion und endoprothetische Versorgung des Kniegelenks mit einer individuellen Tumorendoprothese der Firma „Inmed“). Entsprechend dem Behandlungsprotokoll von Osteosarkomen wurden dem Patienten 5 Zyklen einer präoperativen Polychemotherapie und 7 Zyklen einer postoperativen Polychemotherapie intravenös verabreicht. Im Februar 2020 war er auf einer Treppe ausgerutscht, hörte ein knackendes Geräusch und fühlte einen jähen Schmerz im Bereich des rechten Hüftgelenks, wonach er sich auf die rechte untere Extremität nicht stützen konnte. Nach Anfertigung einer Röntgenaufnahme wurde eine pathologische Femurfraktur an der Stelle, wo die Endoprothese mit ihrem Schaft in den Oberschenkelknochen eingepflanzt wird, diagnostiziert. Am 20.02.2020 wurde eine Metallosteosynthese am rechten proximalen Femur mittels einer DHS-Platte, Schrauben und Cerclagen durchgeführt. Die postoperative Periode verlief ohne Komplikationen. Die Verlaufskontrolle zeigt nach dem Stand vom August 2020, dass die Patientin ein gutes Allgemeinbefinden hat. Klinisch und röntgenologisch zeigt sich eine stabile Metallosteosynthese, es ist eine langsame der Femurfraktur zu erkennen. In Abbildung 2 sind die Röntgenaufnahmen nach der Endoprothesenversorgung des Patienten M. dargestellt, auf denen die Femurfraktur und der Zustand nach einer Metallosteosynthese mit einer Knochenplatte und Cerclagen zu erkennen sind.

Fazit. Aufgrund der Ergebnisse unserer Studie lässt sich feststellen, dass die Verwendung von individuellen Tumorendoprothesen bei Knochentumoren im Bereich des Kniegelenks das grundlegende chirurgische Behandlungsverfahren für diese Pathologie darstellt. Aus dem Vergleich zweier Endoprothesenkonstruktionen – der individuellen Tumorendoprothesen und der individuellen modularen Tumorendoprothesen – ergibt sich, dass sich die periprothetische Infektion, die aseptische Lockerung des Endoprothesenschaftes, der Knochenbruch an der Stelle, wo die Endoprothese mit ihrem Schaft eingepflanzt wird, und der Endoprothesenbruch als Hauptkomplikationen nach der Implantation von Tumorendoprothesen erwiesen. Pathologische Frakturen bei einem Tumor in der

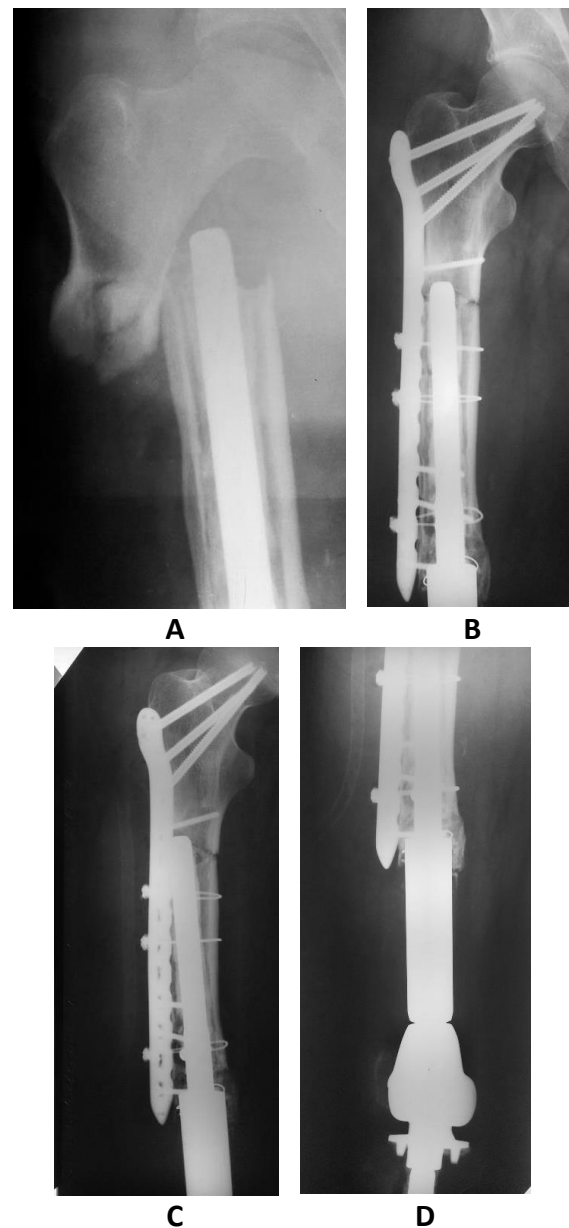


Abbildung 2 Röntgenaufnahmen nach Endoprothetik des Kniegelenks beim Patienten M.: a) Femurfraktur erkennbar; b), c) und d) Zustand nach einer Metallosteosynthese mit einer Knochenplatte und Cerclagen.

präoperativen Phase, verschiedene chirurgische Eingriffe in der präoperativen Phase, eine intraarterielle oder intravenöse Polychemotherapie sowie eine Strahlentherapie in der prä- und postoperativen Phase, die Tumoralokalisation, ein großer Knochendefekt nach der Resektion, eine übergroße Endoprothese, Defizit an Weichgewebe für die Abdeckung einer Endoprothese, Übergewicht, Begleiterkrankungen (Osteoporose, Diabetes mellitus u. a.), Tumorrückfälle und Nichteinhaltung des empfohlenen orthopädischen Regimes erhöhen nachweislich das Risiko für eine aseptische Lockerung der Endoprothese und einen Knochenbruch im

Bereich des Endoprothesenschaftes.

Schlussfolgerungen.

1. Die aseptische Endoprothesenlockerung und die Knochenbrüche im Bereich des Endoprothesenschaftes sind durch eine Reihe von präoperativen Ursachen bedingt, deren Ausschaltung zu einer effizienten endoprothetischen Versorgung bei Knochentumoren führt. Die aseptische Endoprothesenlockerung und die Knochenbrüche im Bereich des Endoprothesenschaftes können im gleichen Maße sowohl Ursache als auch Folge voneinander sein, dennoch sind sie immer primär gegenüber eitrigen-entzündlichen Komplikationen, die in der späten postoperativen Phase entstanden sind.

2. Die aseptische Lockerung der Endoprothesenkomponenten oder periprothetische Frakturen sind am öftesten mit der Nichteinhaltung des empfohlenen orthopädischen Regimes, einem Trauma oder einem Tumorrezidiv verbunden.

3. Es wurde ein deutlicher Zusammenhang zwischen den periprothetischen aseptischen Komplikationen und der Chemo-, Hormon- oder der lokalen Strahlentherapie, die der Patient in der prä- und postoperativen Phase erhält.

Interessenkonflikt. Diese Publikation stellt keinen Interessenkonflikt zwischen den Autoren dar und ist weder Gegenstand kommerzieller Interessen noch Gegenstand der Vergütung jeglicher Art – sowohl gegenwärtig als auch künftig.

Literatur.

1. *Statistics of cancer in Ukraine // Bulletin of national cancer-register in Ukraine. «Cancer in Ukraine». 2017-2018;20:101.*

2. Santini-Araujo E, Kalil RK, Bertoni F, Park Y-K (Eds.). *Tumors and Tumor-Like Lesions of Bone. Springer Nature Switzerland AG; 2020. Doi: 10.1007/978-3-030-28315-5.*

3. Protsenko VV, Duda BS. *Complications after endoprosthesis of knee joint with individual oncological prothesis at patients with bone tumors* Travma. 2014;15(5):70-74.

4. Cortes EP, Holland JF, Wang JJ, et al. *The Classic: amputation and adriamycin in primary osteosarcoma. Clin Orthop Relat Res. 2005;438:5-8*

5. Klimovitsky VG, Babosha VA, Grebenyuk YA, and others. *Indications and contraindications for endoprosthetics of tumor defects in the knee bones. Trauma. 2014;15(4):42-45.*

6. Wu J, Zhu D, Wang Janjun, et al.

Periprosthetic femoral fractures around tumor endoprotheses treated with limited revision surgery combined with allograft (A case report). Medicine. 2019;98:13. DOI: 10.1097/MD.00000000000015018.

7. Fritzsche H, Hofbauer C, Winkler D, et al. *Komplikations management nach Tumor endoprothesen. Orthopäde. 2019;48:588-97. Doi: 10.1007/s00132-019-03756-z.*

8. Ivanov PP. *Revision surgical interventions for periprosthetic knee infection (Literature review). Department of Traumatology and Orthopedics. 2017;1(21):38-46.*

9. Höll S, Schlomberg A, Gosheger G, et al. *Distal femur and proximal tibia replacement with megaprosthesis in revision knee arthroplasty: a limb-saving procedure. Knee Surg Sports Traumatol Arthrosc. 2012;20:2513-2518.*

10. Grimer RJ, Aydin BK, Wafa H, et al. *Very longterm outcomes after endoprosthetic replacement for malignant tumours of bone. Bone Joint J. 2016;98(B): 857-64.*

11. Bus MPA, van de Sande MAJ, Fiocco M, et al. *What are the long-term results of MUTARS modular endoprotheses for reconstruction of tumor resection of the distal femur and proximal tibia. Clin Orthop Relat Res. 2017;475(3):708-18.*

12. Protsenko VV. *Advantages of modular knee arthroplasty in patients with bone tumors. Oncology. 2015;17(2):129-33.*

13. Röhner E, Windisch C, Nuetzmann K, et al. *Unsatisfactory outcome of arthrodesis performed after septic failure of revision total knee arthroplasty. J Bone Joint Surg Am. 2015;97:298-301. <http://dx.doi.org/10.2106/JBJS.N.00834>.*

14. Henderson ER, Groundland JR, Pala E, et al. *Failure mode classification for tumor endoprotheses: retrospective review of five institutions and a literature review. J Bone Joint Surg Am. 2011;93(5): 418-29. doi: 10.2106/JBJS.J.00834.*

15. Davis AM, Bell RS, Badley EM, et al. *Evaluating functional outcome in patients with lower extremity sarcoma. Clin Orthop Relat Res. 1999;358:90-100.*

16. Kotz RI. *Progress in musculoskeletal oncology from 1922–2012. Int Orthop. 2014;38: 1113-22.*

17. Piccioli A, Rossi B, Sacchetti FM, et al. *Fractures in bone tumour prosthesis (Review article). International Orthopaedics (SICOT). 2015;39:1981-87. DOI 10.1007/s00264-015-2956-7.*

Naboychenko Ya.V.*Kharkiv National Medical University, Ukraine***Zamiatin P.M.***DU "Institute of General and Emergency Surgery named after V.T. Zaitsev to NAMS of Ukraine"*

REGULARITIES OF MORPHOGENESIS OF INTERNAL FEMALE GENITAL ORGANS IN THE PERINATAL PERIOD OF ONTOGENESIS

Abstract. *The aim. Improving the results of surgical treatment of patients with pseudocysts of the pancreas by conducting a comparative analysis of the development of free radical processes in the body depending on the degree of formation of pseudocysts of the pancreas. Materials and methods. The analysis of examination and treatment of 101 patients was performed. All patients with SCI were divided into 2 clinical groups - the main and the comparison group. The main group includes 39 (48.43%) patients who were treated in the surgical department of the city clinical hospital №17 from 2015 to 2020. The comparison group included 62 (51.57%) patients who in the period 2009-2014, traditional medical and diagnostic tactics were used. Results and discussion. A comparative analysis of the peculiarities of the development of free radical processes of the organism depending on the degree of formation of the pseudocyst of the pancreas. Conclusions. The value of glutathione reductase and malonic dialdehyde (MDA) at different degrees of cyst wall formation was established. It has been observed that the toxic effect of free radical oxidation products helps to maintain the inflammatory reaction and tissue ischemia in patients with unformed pseudocysts of the pancreas.*

Key words: *pancreatic pseudocysts, glutathione, malonic dialdehyde, free radical oxidation.*

Pseudocysts of the pancreas are the most common variant of local complications of acute pancreatitis, accounting for 50-92% in destructive forms [1, 2]. In 81% of cases, pseudocysts have a complicated course [3]. This is due to insufficiently developed diagnosis and lack of criteria for choosing tactics of treatment of these patients. The question of treatment of patients with pseudocysts of the pancreas is considered complex and unresolved [4]. Traditionally, patients with pseudocysts of the pancreas use waiting tactics [5], but it is during this time there are life-threatening complications [6] in the form of suppuration of the cyst, bleeding, violation of the integrity of the cyst wall, compression of hollow organs, gastric obstruction tract and portal hypertension [7].

The aim of the work is to study the peculiarities of the development of free radical processes of the organism depending on the degree of formation of the pseudocyst of the pancreas.

Materials and methods of research. The analysis of examination and treatment of 101 patients was performed. All patients with SCI were

divided into 2 clinical groups - the main and the comparison group. The main group includes 39 (48.43%) patients who were treated in the surgical department of the city clinical hospital №17 from 2015 to 2020. The comparison group included 62 (51.57%) patients who in the period 2009-2014, traditional medical and diagnostic tactics were used. To conduct a comparative analysis and obtain more reliable results of the study, a control group consisting of 25 conditionally healthy examined volunteers, residents of the Kharkiv region, was additionally introduced. Groups of patients were representative by sex, age, baseline clinical and laboratory parameters. The localization and average size of the pseudocyst are presented in table. 1.

The set of diagnostic measures included fibroesophagogastroduodenoscopy (FEGDS), ultrasound (US), computed tomography (CT), endoscopic retrograde cholangiopancreatography (ERCP), as well as biochemical examination of cysts. Diagnosis of the disease was performed on the clinical symptom complex, according to instrumental and laboratory tests. Studies in

Table 1

Localization and average size of pseudocysts of the pancreas ($M \pm \sigma$)

Indicator	Localization of pseudocysts in the pancreas			
	Head	Body I	Body-Tail I	Tail
Number of patients	30	4	10	32
The average size of the pseudocyst, mm	44,8±5,6	45,2±9,8	55,4±9,8	66,1±9,4

patients were performed with informed consent in accordance with the ethical standards regulated by the Declaration of Helsinki in 2000. The content (MDA) in mmol / l was evaluated by color reaction with 2-thiobarbituric acid in the presence of trichloroacetic acid by the method of ID Steel (1977). The glutathione content was determined in mmol / l by the method of S. Sedlak, R. Lindsey (1968). The activity of glutathione reductase was evaluated (in mmol / h • l) by its ability to oxidize NADPH at a wavelength of 340 nm E. Racker (1955). The activity of glucose-6-phosphate dehydrogenase (in μ mol / h • l) was evaluated according to the method of Yu.Ya. Zechariah. The uric acid content (in μ mol / l) was determined by the method of G. Oteta et al. (1976).

The results of the study and their discussion.

In order to identify the clinical features of pseudocysts of the pancreas of varying degrees of formation and their complications, we conducted a comparative assessment of the symptoms

observed in patients seeking medical attention (Tab. 2).

The presence of any of these symptoms, taking into account the anamnestic data on the episode of acute pancreatitis was an indication for diagnostic measures to clarify the diagnosis. All patients with pseudocysts of the pancreas underwent esophagogastroduodenoscopy (EGDS). Extrahepatic portal hypertension syndrome, which was detected in 10 (15.4%) patients, was manifested by varicose veins of the stomach and esophagus, and in 4 cases - ascites. The reason for this was the compression of the veins of the portal system by a cyst, as well as thrombosis of the splenic artery in unformed pseudocysts (SA Starostin, 1999). In 4 (6.15%) patients during ERCP biliary hypertension was detected, of which two (3.08%) patients had mechanical jaundice. Compression deformation of the lumen of the stomach and duodenum of varying severity was observed in 47 (50.8%) patients with pseudocysts of the pancreas.

Table 2

Frequency of clinical symptoms in pseudocysts of the pancreas

The studied sign	Unformed pseudocysts (n=45)	Formed pseudocysts (n=39)	Purulent pseudocysts (n=6)	χ^2	p
Pain	39 (96,67%)	36 (89,67%)	6 (100%)	1,689	0,430
Nausea	14 (46,67%)	13 (44,83%)	3 (50%)	0,059	0,971
Vomit	7 (23,33%)	3 (10,35%)	1 (16,67%)	1,770	0,413
Jaundice	3 (10%)	0	1 (16,67%)	0,56	0,613
Subfebrile	11 (36,67%)	4 (13,79%)	5 (83,33%)	12,196	0,002

Table 3

Endoscopic picture of the mucous membrane of the stomach and duodenum in postnecrotic pseudocysts of the pancreas

The nature of the pathology	Unformed pseudocysts (n=45)	Formed pseudocysts (n=39)	χ^2	p
Erythema of the gastric mucosa	45 (100%)	36 (86,67%)	10,824	0,001
Swelling of the gastric mucosa	18 (51,43%)	7 (23,33%)	4,266	0,039
Cyanosis of the mucous membrane	11 (31,43%)	3 (10%)	3,213	0,073
Erosion of the stomach	6 (17,14%)	3 (10%)	0,222	0,638
Duodenitis	34 (97,14%)	20 (66,67%)	8,614	0,003
Papillitis	13 (37,14%)	3 (10%)	5,034	0,025

Irrespective of localization at the size of a pseudocyst of a pancreas more than 45 mm (19 patients) at all patients deformation of a gleam of a stomach due to its compression from outside, explosion of a back wall of a stomach, a hyperplasia of folds of a stomach, deformation of a bulb and narrowing of a descending branch of a duodenum was defined. Changes in the mucous membrane in the areas adjacent to the cyst, had differences depending on the formation of the pseudocyst, and are presented in table. 3.

The study convincingly demonstrated the importance of functional and morphological changes in the stomach and duodenum, which revealed endoscopic methods in the pseudocysts of the pancreas. It was found that the processes of free radical evaluation are more intense in unformed pseudocysts of the pancreas, as evidenced by an increase in MDA in blood plasma and erythrocytes than in groups of people with formed pseudocysts, also in control. It was found that the activity of glutathione reductase in the blood was lowest in people with unformed postnecrotic cysts of the pancreas. There was also significant use of the activity of G-6-FDG - the main cycle of the enzyme pentose phosphates, which catalyzes the formation of reduced equivalents in unformed pseudocysts of pancreatic debt due to the formed pseudocysts of the pancreas. There was an inverse correlation between the content of malonic dialdehyde and glutathione in erythrocytes (Spearman correlation coefficient $r = -0.896$, $p < 0.01$). Thus, the intensification of lipid peroxidation processes in unformed pseudocysts of the pancreas occurs against the background of the formation of such components of the endogenous antioxidant system as glutathione and glutathione reductase.

Conclusions. The studied indicators can serve as markers in determining the optimal timing of the formation of the physical strength of the pseudocyst wall, sufficient for the imposition of a cystodegestive anastomosis. Blood glutathione

reductase activity was lowest ($r = 0.883$; $p < 0.05$) in patients with unformed postnecrotic pancreatic cysts, regardless of the thickness of the cyst wall, because it indicates that the cyst wall is not strong enough.

In order to predict infection of the cystodegestive anastomosis area, it is possible to use the determination of G-6-FDG activity, glutathione reductase and glutathione indicators as markers of prognosis of early postoperative complications.

References

1. DiMaio CJ. Management of complications of acute pancreatitis. *Curr Opin Gastroenterol.* 2018 Sep;34(5):36-42.
2. Desyaterik VI, Krikun MS. Zmini klinichnih pidhodiv ta likuval'noi taktiki pri gostromu pankreatiti u svitli pereglyanutoi klasifikacii Atlanta 2012. *Klinichna hirurgiya.* 2017;3:51-5 [In Ukr.].
3. Larrey Ruiz L, Luján Sanchis M, Peño Muñoz L, Barber Hueso C, Cors Ferrando R, Durá Ayet AB, et al. Pseudoaneurysm associated with complicated pancreatic pseudocysts. *J. Rev Esp Enferm Dig.* 2016;108(9):583-5.
4. Santhi Swaroop Vege, David C. Whitcomb, Shilpa Grover. Management of acute pancreatitis. Literature review current through:2018. This topic last updated: Apr 12, 2018, 12-14.
5. Pidgirnij BYA. Perekhresni mekhanizmi zapalennya i gemostazu v likuvanni hvorih na gostrij pankreatit [disertaciya]. Uzhgorod: Uzhgorods'kij nac. un-t;2017.21 s. [In Ukr.].
6. Rajendran P., Nandakumar N., Rengarajan T., Palaniswami R., Gnanadhas E. N., Lakshminarasiah U. Antioxidants and human diseases. *Clinica Chimica Acta.* 2014;436:332–347. 32-34.
7. Deponte M. Glutathione catalysis and the reaction mechanism of glutathione-dependent enzymes. *Biochimica et Biophysica Acta.* 1830;2013:317–326.

CONTENT:

Pohorielova O.O., Shevchenko O.S. DEPENDENCE OF HUMAN-BETA-DEFENSIN-1 LEVEL ON DRUG-RESISTANCE SPECTRUM AND TREATMENT REGIMENS IN PATIENTS WITH PULMONARY TUBERCULOSIS	2
Fridman R. A COMPARISON OF DEEP NEURAL NETWORK ARCHITECTURES FOR ARRHYTHMIA CLASSIFICATION	7
Sahan V. TOWARDS THE ECG-BASED BIOMARKERS OF HUMAN AGING	15
Yuzko R.V., Slobodian O.M. PECULIARITIES OF PERINATAL TOPOGRAPHY OF THE HEPATODUODENAL LIGAMENT COMPONENTS	22
Malynovskyi A. MOBILE SYSTEM FOR ECG SIGNALS COLLECTION AND PROCESSING IN REAL-TIME	27
Burianov O.A., Prozenko V.V., Obada Muhammad Bishtawi, Solonizyn J.O., Solovyov I.O. ANALYSE VON ASEPTISCHEN PERIPROTHETISCHEN KOMPLIKATIONEN BEI KNIEGELENKSTUMOREN JE NACH ART DER KNIEGELENKSENDOPROTHESE	35
Naboychenko Ya.V., Zamiatin P.M. REGULARITIES OF MORPHOGENESIS OF INTERNAL FEMALE GENITAL ORGANS IN THE PERINATAL PERIOD OF ONTOGENESIS	44



Deutscher Wissenschaftsherold German Science Herald

Bibliographic information published by the Deutsche Nationalbibliothek
The Deutsche Nationalbibliothek lists this publication in the Deutsche Nationalbibliografie; detailed
bibliographic data are available on the Internet at <http://dnb.dnb.de>

№ 4/2019 – 10

Passed in press in November 2019



WirmachenDruck.de

Sie sparen, wir drucken!



Berlin

